



UWL REPOSITORY
repository.uwl.ac.uk

Numerical modeling and parametric analysis of thermal performance for the large-scale seasonal thermal energy storage

Xu, Guozhi, Hu, Lei, Luo, Yongqiang, Tian, Zhiyong, Deng, Jie ORCID logo ORCID: <https://orcid.org/0000-0001-6896-8622>, Yuan, Guofeng and Fan, Jianhua (2022) Numerical modeling and parametric analysis of thermal performance for the large-scale seasonal thermal energy storage. *Energy and Buildings*, 275. p. 112459. ISSN 0378-7788

<http://dx.doi.org/10.1016/j.enbuild.2022.112459>

This is the Accepted Version of the final output.

UWL repository link: <https://repository.uwl.ac.uk/id/eprint/9397/>

Alternative formats: If you require this document in an alternative format, please contact: open.research@uwl.ac.uk

Copyright: Creative Commons: Attribution-Noncommercial-No Derivative Works 4.0

Copyright and moral rights for the publications made accessible in the public portal are retained by the authors and/or other copyright owners and it is a condition of accessing publications that users recognise and abide by the legal requirements associated with these rights.

Take down policy: If you believe that this document breaches copyright, please contact us at open.research@uwl.ac.uk providing details, and we will remove access to the work immediately and investigate your claim.

Rights Retention Statement:

Journal Pre-proofs

Numerical modeling and parametric analysis of thermal performance for the large-scale seasonal thermal energy storage

Guozhi Xu, Lei Hu, Yongqiang Luo, Zhiyong Tian, Jie Deng, Guofeng Yuan, Jianhua Fan

PII: S0378-7788(22)00630-2
DOI: <https://doi.org/10.1016/j.enbuild.2022.112459>
Reference: ENB 112459

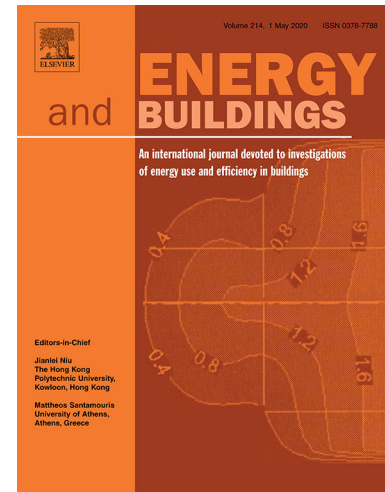
To appear in: *Energy & Buildings*

Received Date: 13 July 2022
Revised Date: 30 August 2022
Accepted Date: 7 September 2022

Please cite this article as: G. Xu, L. Hu, Y. Luo, Z. Tian, J. Deng, G. Yuan, J. Fan, Numerical modeling and parametric analysis of thermal performance for the large-scale seasonal thermal energy storage, *Energy & Buildings* (2022), doi: <https://doi.org/10.1016/j.enbuild.2022.112459>

This is a PDF file of an article that has undergone enhancements after acceptance, such as the addition of a cover page and metadata, and formatting for readability, but it is not yet the definitive version of record. This version will undergo additional copyediting, typesetting and review before it is published in its final form, but we are providing this version to give early visibility of the article. Please note that, during the production process, errors may be discovered which could affect the content, and all legal disclaimers that apply to the journal pertain.

© 2022 Published by Elsevier B.V.



Numerical modeling and parametric analysis of thermal performance for the large-scale seasonal thermal energy storage

Guozhi Xu¹, Lei Hu², Yongqiang Luo*¹, Zhiyong Tian¹, Jie Deng³, Guofeng Yuan⁴, Jianhua Fan⁵

1 School of Environmental Science and Engineering, Huazhong University of Science and Technology, Wuhan, 430074, China

2 CITIC General Institute of Architecture Design and Research Co., Ltd., Wuhan, 430074, China

3 School of Computing and Engineering, University of West London St Mary's Road, Ealing London, W5 5RF, UK

4 Institute of Electrical Engineering Chinese Academy of Sciences, Beijing 100190, China

5 Department of Civil and Mechanical Engineering, Technical University of Denmark, Brovej 118, 2800 Kgs. Lyngby, Denmark

Corresponding Author: luoroger@yeah.net yqluo@hust.edu.cn (Y. Luo)

Highlights

- A numerical model is proposed for seasonal thermal energy storage (STES) couple with solar collector
- The model is featured as relatively high computational speed and accuracy
- An analysis on technical planning and operational design for the STES is offered
- The key parameters for system design and control are investigated with instructive results

ABSTRACT :

Seasonal **thermal** energy storage (STES) systems are a key component in expanding the share of renewables in energy programs because they provide schedulability and flexibility. However, such a large-scale system requires careful planning to avoid high investment costs. Therefore, numerical models are becoming increasingly important as an alternative. This paper develops a numerical model of STES coupled with solar collector. The model was verified based on the experimental data of the Huangdicheng Project in China. The results show that the relative error in the charging mode and discharging mode is only 1.57% and 0.46%, respectively. Then, the effects of different charging and discharging mode on the heat storage efficiency of the tank and the efficiency of solar collector systems in STES were studied. The study found that in the initial charging stage, the water temperature rise curve caused by different flow rates is very different. In the design of the collector-storage area ratio, the relatively economical collector-storage ratio of this model is around 3768L/m². The selection of different proportions of discharging energy in the discharge stage has a great impact on the heat storage efficiency of the system in the next year. Moreover, the influence of different depth-diameter ratios of the tank on the system heat storage efficiency is discussed in detail, which has important guiding significance for model application and system analysis. **This paper provides some references for the scale design and operation optimization of cylindrical STES.**

Keywords:

Seasonal thermal energy storage, Numerical model, Climate, Depth-diameter ratio, Collector-Storage ratio

36 **1. Introduction**

37 Heat shortage and smog pollution are inevitable problems in traditional heating systems, especially in
38 underdeveloped areas [1]. Seasonal thermal energy storage (STES) is therefore essential for district heating systems
39 as they can flexibly integrate various fluctuating renewable energy sources [2-4]. Some ambitious targets are
40 proposed in the Portugal National Energy and Climate Plan 2030 (NECP 2030) and the Roadmap for Carbon
41 Neutrality 2050 (RCN 2050). Due to its wide distribution and huge reserves, solar energy is a promising renewable
42 energy, which will play an important role in carbon neutralization. Considering that the building energy consumption
43 accounts for 21% of the total commodity energy consumption, and the space heating consumes 21% of the building
44 energy, it is natural and necessary to develop a solar District heating(SDH) technology suitable for buildings, which
45 is also in line with the proposal of clean heating in northern China[5,6]-[5-7].

46 According to the different storage media, STES can be divided into sensible heat storage, latent heat storage
47 and chemical energy storage [7-11], Among them, sensible heat storage is still the most commonly used type of
48 STES [7] , Concerning STES for SDH systems, four main types exist in commercial applications, including tank
49 TES (TTES), pit TES (PTES), borehole TES (BTES), and aquifer TES (ATES) as shown in **Fig. 1**.

50 PTES are simple systems that store hot water in very large excavated basins with an insulated lid. The sides
51 and bottom are typically covered by polymer liners. The water can also be stored in artificial tanks made of reinforced
52 concrete or stainless steel constructed, so these systems may also be called TTES, However, TTES has some
53 problems, such as high cost, high insulation demand, small volume, etc. BTES are similar to geothermal heat
54 exchange systems with a carrier fluid circulated through a closed-loop pipe network installed in vertical boreholes
55 backfilled with sand bentonite. A key limitation of BTES is their relatively low heat extraction efficiency[12]. ATES
56 systems fill the watertight plastic liner with a gravel-water mixture that serves as the storage material. Heat is charged
57 into and discharged out of the storage medium either by direct water exchange or by plastic piping installed in
58 different layers inside the pool. The gravel-water mixture has a lower specific heat than water alone; therefore, the
59 basin volume has to be approximately 50% larger than an equivalent water pit heat storage system to obtain the same
60 heat storage capacity [11,13]. The PTES is currently the most reliable and widely used seasonal heat storage system.
61 Since the surface area does not increase, a larger amount of storage increases storage efficiency [13,14].The
62 operating parameters of some STES are given in **Table 1**.

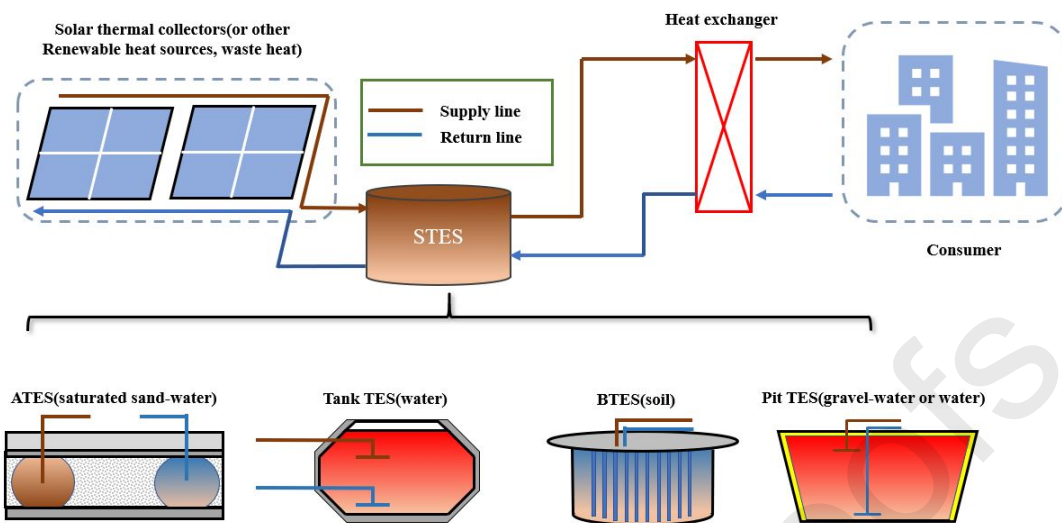


Fig 1 Four types of seasonal sensible heat storage systems

Table 1

STES operating parameters

Location	Building time	Volume(m ³)	Heist Temperature (°C)	Total heat loss (%/MWh /a)
Lambohov	1980	10000	70	40 / 250
Herlev	1991	3000	85	- / 80
Ottrupgaard	1995	1500	60	30 / 85
Marstal	2012	75000	85	48 / 2908
Dronninglund	2013	62000	85	41 / 2260
Huangdicheng	2018	3000	67	38/62

Current simulation tools for PTES can be divided into three categories: (a) computational fluid dynamics (CFD) for part-level modeling, (b) simplified 2D/3D numerical methods for system-level modeling and (c) Long-time multi-system coupling research on STES system by using software such as TRNSYS et al. CFD/COMSOL has been widely used in detailed studies of PTES, where almost all factors can be considered in such numerical models, including the thermal properties of storage, design and geometry, surrounding soil conditions, and heat and mass transfer mechanisms[15-17].

Fan et al. developed a CFD model to simulate the real-scale PTES in Marstal (75,000 m³). Several typical operation conditions were considered in the investigations to study the thermal performance of both the storage and the surrounding soil region [18]. Bai developed a finite-difference model to study the water storage and thermal stratification of a 3000 m³ underground pit in Huangdicheng, which was validated with experimental data[13]. Based on the Seasonal Ground Heat Storage (XST) model in TRNSYS, Pan et al. proposed an improved two-dimensional model to experimentally and theoretically study the long-term thermal properties of 60,000 m³ PTES in Dronninglund, and analyzed the five-year measurement results to study development of temperatures, heat flows, and thermal stratification in heat storage[15].

Calculations using software such as CFD/COMSOL are usually very time-consuming; therefore, all these studies are either based on short-term analyses or only consider as ~~aan alternate modes~~ alternate mode. CFD/COMSOL studies of STES are impractical in most cases. But for PTES, some parameters change over several

86 months. Generally, it takes four to six years for a pit to reach a steady state. On the other hand, as part of the SDH,
 87 the simulation of the energy system should take into account the effects of relevant components such as solar fields,
 88 heat pumps and district heating (DH) networks [19]. The current CFD/COMSOL simulation, as an independent
 89 model, is too complex to build a compatible platform to calculate the thermal performance of the system.

90 The engineering equation solver (EES) tools are widely used for system-level simulation. In these models, the
 91 PTE is simplified to reduce the computational effort. However, these simplified models either simplify the water
 92 region in the pit or simplify the boundary conditions of the soil region, which will cause the model to deviate from
 93 the real operating conditions. M.jradi et al employed the lumped capacity models to calculate buried STES, which
 94 usually neglects the inner water temperature distribution in the storage[20]; Kubinski et al. built a fully hybrid PTES
 95 dynamic model to calculate the overall thermal performance of the Vojens SDH system in Denmark. This also differs
 96 far from the actual situation[21].

97 The TRNSYS environment is widely used to carry out system-level simulations due to its vast component
 98 library. Several coarse models were developed for buried TES, such as XST, Ice Pit thermal energy storage (ICEPIT),
 99 and Under-Ground Seasonal Thermal Storage (UGSTS) models. S.Raab et al, integrated the validated XST-model
 100 into a TRNSYS model to calculate the thermal behavior of the solar assisted district heating system in Hannover in
 101 2002. The deviations between measured and calculated heat quantities do not exceed 5%[22].Pan et al, carried out a
 102 modified 2D model to calculate the thermal performance of the large-scale PTES based on the XST model in
 103 TRNSYS. The results showed that the developed model predicts well the storage temperatures and the heat flows[15].
 104 But considering the details of STES and the entire DSH system, it is not easy to perform coupled simulations over
 105 the long term. Since only a few large-scale PTES are running, it is difficult to validate and modify existing models
 106 due to limited experimental data.

107 In the literature review, it can be seen that related research either simplifies the calculation of soil region or
 108 water region in the STES model to achieve rapid analysis, but this simplification is often deviated from reality.
 109 However, when using computational fluid dynamics software such as CFD/COMSOL for simulation, large time
 110 scale simulation becomes a luxury. Due to the complexity of components, TRNSYS software also requires careful
 111 control and a lot of time when running and analyzing STES.

112 Therefore, in this study, we propose a simplified numerical model that can be used to describe the operation of
 113 STES considering the solar collector component, the pit domain including the water region and surrounding soil
 114 region, and the heating component. Through this study, a comprehensive discussion of the influence of different
 115 parameters on STES is carried out for a 10000m³ cylindrical pit. In the charging mode, we discuss in detail the
 116 influence of the input end about the input flow and collector area on the heat storage efficiency of the system; In the
 117 discharging mode, we carefully analyzed the influence of the output end on the heat storage performance of the
 118 system with respect to the flow, heating temperature difference and operation duration. This may guide a better
 119 design and control of STES in further research and practice. and an in-depth understanding of the limitations and
 120 improvements of the model is provided to provide a reference for the rapid planning and design of the STES. It will
 121 also provide useful tools and guidance to further promote the development of STES.

122 2. Method and model

123 2.1. Overview of methods

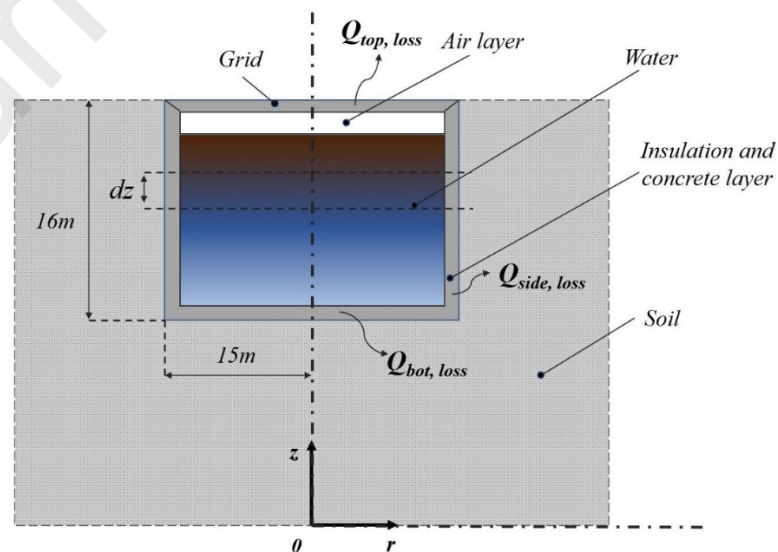
124 Since the heat transfer between the water and the surrounding soil in a STES belongs to different domains, their
 125 temperature field solutions should be solved separately. The control equations and boundary conditions are different,

126 and once the analytical results of these two components are obtained, the overall simulation of the STES system can
 127 be performed by connecting the heat transfer of water and soil through the temperature boundary of the pool wall.
 128 For the soil heat transfer, the pool heat flow is used as the heat source and the soil temperature can be updated by
 129 time step simulation. Then, for the heat transfer in the pool water, the updated soil temperature can be used as an
 130 important thermal boundary for the water heat transfer. In the model building and calculation a one-dimensional heat
 131 transfer model is used for the water body model in STES, and a two-dimensional heat transfer model is used for the
 132 soil heat transfer.

133 Considering the one-dimensional heat transfer in the pit water, many previous studies have made important
 134 contributions that paved the way for this research. The current problem with the one-dimensional heat transfer of the
 135 water in the pool is that the pure one-dimensional heat transfer between the layers of the water body have inconsistent
 136 heat dissipation rate, it is difficult to avoid the situation where the lower water body is hotter than the upper water
 137 body, which is not in line with the reality of the situation. Considering the heat transfer in water region inside the
 138 pool, lots of studies previously made critical contributions which paved the way for this study. Dahash et al neglected
 139 this item in the one-dimensional heat transfer model of the pool, which is suitable for simulation in the charge mode
 140 of the pool when the top is well insulated or even adiabatic[23]. Fabian Ochs et al proposed to replace the water
 141 thermal conductivity term in order to improve the thermal conductivity of water and thus exclude the inverse
 142 thermocline[24]. The method used in this paper to deal with the anti-thermocline is to calculate the temperature
 143 sequence of each layer of the water within one-time step. For the place where the bottom layer temperature is higher
 144 than the upper layer water, the two layers of water are fused into an isothermal layer, and are checked and calculated
 145 from the bottom layer of the pit at one time-step, this is reasonable in practice. Theoretically, when the water
 146 temperature in the lower layer is higher than that in the upper layer, they will be mixed under the action of gravity
 147 until the temperature is the same. It should be noted that this mixing takes time, so it has certain requirements for
 148 the calculated time step and the calculated water layer volume

149 Due to the cylindrical shape of the pit, it can be regarded as a two-dimensional rotational symmetrical figure to
 150 deal with the heat transfer of the soil.

151 Finally, the numerical model outside and inside the pool are incorporated with the solar collector model. It
 152 should be noted that within each time step, steady state heat transfer model of fluid is solved and the pool wall
 153 temperature is updated by transient soil heat transfer model, because the time step usually is one hour, which is
 154 sufficient for fluid to reach steady state within this time interval.



155

156

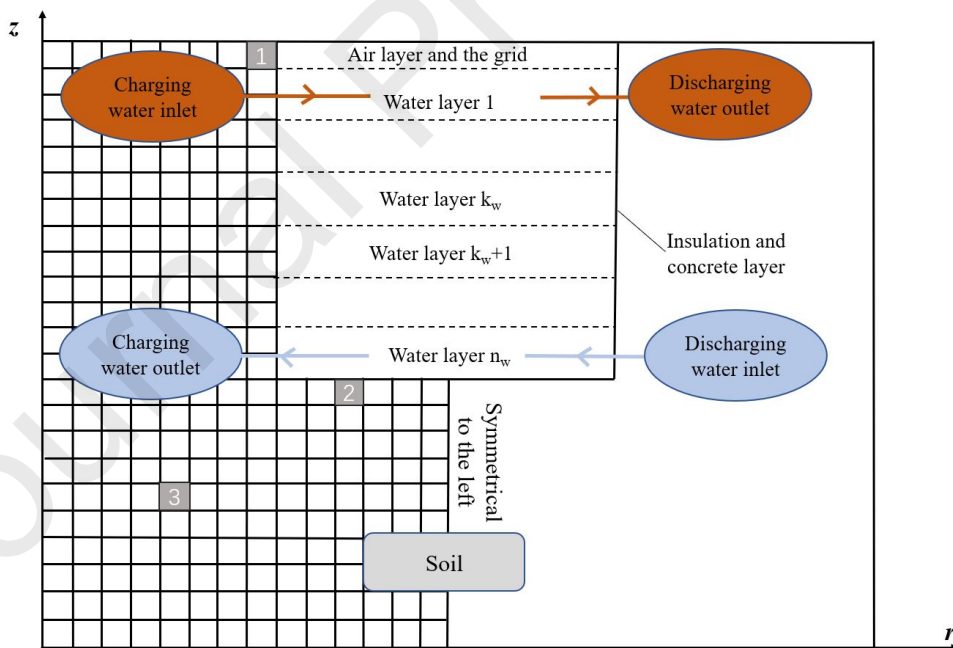
Fig 2 Schematic of STES

157 2.2. Numerical analysis

158 Based on the following assumptions, a simplified numerical model of a cylindrical underground pit with a
 159 radius of 15m, a depth of 16m and a total volume of 11304m³ was developed for rapid calculation, as shown in **Fig.**
 160 **2:**

- 161 1) There is no scale or impurity on the surface of the pit that reduces the heat transfer rate.
 162 2) The soil is homogeneous, and the influence of groundwater seepage and other factors on heat transfer is not
 163 considered.
 164 3) The influence of temperature on physical parameters of the water is not considered.
 165 4) The water in the pit at each height has the same temperature, and there is no temperature gradient in the
 166 radial direction [13,25].
 167 5) The cover board has the same temperature, and there is no temperature gradient in the radial direction.
 168 6) There is an air layer between the cover and the water surface. Due to sealing, the latent heat of water
 169 evaporation is small, and the air ~~does not flow~~ **hardly flows**, which is similar to solid heat transfer [13].
 170 7) There are thermal insulation layer and concrete layer on the wall of the pool. Since the two are very small
 171 compared with the pool diameter, their physical properties are only used for calculating the thermal resistance.
 172 8) Due to the symmetry of the cylinder, this paper takes half of the model to study.

173 2.2.1. Grid scheme



174

175 **Fig 3** Mesh for the STES (1, 2 and 3 are typical heat transfer calculation units of the soil region)

176

177 With these assumptions, the water region with one top air layer in the STES can be simplified into a one-
 178 dimensional model and a two-dimensional model of soil and concrete wall. There is an air layer of 0.3m thickness
 179 above the water in the pit. Above the air layer is a cover board of 0.3m thickness with thermal insulation property.
 180 The surrounding and bottom of the pool are built by a layer of 0.3m thick concrete layer. The water region is divided

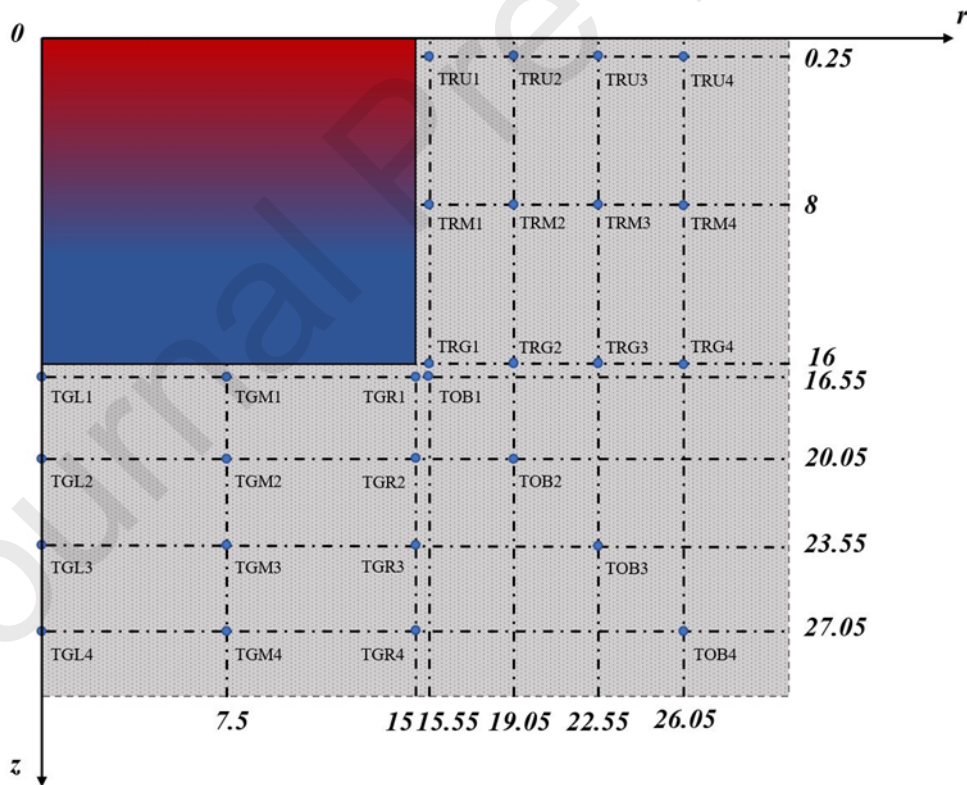
181 into n_w nodes on average. The nodes in the water layer are numbered from 1 to n_w from top to bottom, as shown
 182 in Fig. 3.

183 Compared with the diameter r and depth d of the STES, the thickness of the air layer, cover board and concrete
 184 layer is very small. So that when meshing, the physical existence is ignored, and it is only used as thermal resistance
 185 in heat transfer calculation.

$$186 \quad R_a = \frac{\delta_a}{\lambda_a}, R_g = \frac{\delta_g}{\lambda_g}, R_{con} = \frac{\delta_{con}}{\lambda_{con}} \quad (1)$$

187 In order to facilitate the mesh division, a consistent mesh is used to divide the soil area within the one-year
 188 operation cycle. According to the needs of saving computing resources, or the change law of temperature gradient,
 189 a near dense and far sparse mesh can be set.

190 The heat loss from the pit can affect the temperature of a large amount of the surrounding soil. The radius of
 191 the soil area is 15m and the depth under the pit is also 15m to simulate the semi-infinite soil region. Therefore, the
 192 total radius of the whole calculation domain is $Rad = r + 15 = 30m$, and the total depth is $Dep = H + 15 = 31m$.
 193 Temperature measuring points shall be arranged at the side, bottom and inclined bottom of the pit, as shown in Fig.
 194 4, the location and definition of temperature measuring points is listed in Table 2. The cloud chart of the
 195 measurement results shows that in the first year of operation, the edge area is not affected by the water temperature.
 196 Therefore, it is considered that the soil area is large enough and the semi-infinite boundary is appropriate. In case of
 197 multi-year operation $Rad = 5r; Dep = 5H$.



198
 199 Fig 4 Temperature measuring point of STES
 200
 201

202 Table 2

203 Location and definition of temperature measuring points

Name	Means	Location
TGL1 to TGL4	Temperature measuring point on the bottom left of the pit	As shown in Fig. 4
TGM1 to TGM4	Temperature measuring point on the bottom middle of the pit	As shown in Fig. 4
TGR1 to TGR4	Temperature measuring point on the bottom right of the pit	As shown in Fig. 4
TRU1 to TRU4	Temperature measuring point on the top right of the pit	As shown in Fig. 4
TRM1 to TRM4	Temperature measuring point on the middle right of the pit	As shown in Fig. 4
TRG1 to TRG4	Temperature measuring point on the bottom right of the pit	As shown in Fig. 4
TOB1 to TOB4	Temperature measuring point on the obliquely down of the pit	As shown in Fig. 4

204

205 2.2.2. Water region

206 There is a cover board with thermal insulation between the first layer of water surface and the outside air, and
 207 there is an air layer between the cover plate and the water surface. In the confined space of water surface and cover
 208 plate, the air layer flow is limited. In this case, the heat transfer of latent heat and mass transfer of water gasification
 209 is much smaller than that of sensible heat, so the calculation is ignored [13,26].

210 In the 1-D Pit model, the mass of the water flowing in/out the tank is held conserved and, thus, the steady-state
 211 continuity equation for the water is given as follows:

$$212 \quad m_{in} = m_{out} = m \quad (2)$$

213 Therefore, the heat transfer equation of the first layer of water is calculated as follows:

$$214 \quad \rho_w C_{p,w} V_{w,1} \frac{\partial T_{w,1}}{\partial \tau} = \frac{T_{w,2} - T_{w,1}}{\frac{\Delta H_w}{\lambda_w A_p}} + \frac{T_{ev} - T_{w,1}}{\frac{\delta_a}{\lambda_a A_p} + \frac{1}{h_{ev} A_p} + \frac{\delta_g}{\lambda_g A_p}} + Q_{side-loss,1} + m C_{p,w} \left\{ \begin{array}{l} T_{in} \text{ (when, } m > 0) \\ T_{w,2} \text{ (when, } m < 0) \end{array} \right\} - T_{w,1} \quad (3)$$

215 The heat transfer coefficient between the ambient air and the soil, h_{ev} was calculated using McAdam's formula
 216 [27]

$$217 \quad h_{ev} = \begin{cases} 5.4 + 3.8u, u < 4.9 \text{ m/s} \\ 7.2u^{0.78}, u \geq 4.9 \text{ m/s} \end{cases} \quad (4)$$

218 When the pool is charged, the inlet charging water temperature is calculated by the collector efficiency
 219 formula, and the calculation formula is as follows[28] :

$$220 \quad \eta_c = 0.744 - \frac{4.45(T_{ci} - T_{ev})}{I_g} \quad (5)$$

$$221 \quad Q_c = \text{Sin}\theta A_c I_g \eta_c = m_{in} C_{p,w} (T_{co} - T_{ci}) \quad (6)$$

$$222 \quad T_{co} = T_{in}, T_{ci} = T_{w,n_w} \quad (7)$$

223 Then, the energy equation for k_w ($1 < k_w < n_w$) node in the water region was given by:

$$\begin{aligned}
 & \rho_w C_{p,w} V_{w,k_w} \frac{\partial T_{w,k_w}}{\partial \tau} \\
 224 & = \frac{T_{w,k_w-1} - T_{w,k_w}}{\frac{\Delta H_w}{\lambda_w A_p}} + \frac{T_{w,k_w+1} - T_{w,k_w}}{\frac{\Delta H_w}{\lambda_w A_p}} + Q_{side-loss,k_w} + m C_{p,w} \left(\begin{cases} T_{w,k_w-1} \text{ (when, } m > 0) \\ T_{w,k_w+1} \text{ (when, } m < 0) \end{cases} - T_{w,k_w} \right) \quad (8)
 \end{aligned}$$

225 The energy equation for the bottom node in the water pit was:

$$\begin{aligned}
 & \rho_w C_{p,w} V_{w,n_w} \frac{\partial T_{w,n_w}}{\partial \tau} \\
 226 & = \frac{T_{w,n_w-1} - T_{w,n_w}}{\frac{\Delta H_w}{\lambda_w A_p}} + Q_{bot-loss} + Q_{side-loss,n_w} + m C_{p,w} \left(\begin{cases} T_{w,n_w-1} \text{ (when, } m > 0) \\ T_{in} \text{ (when, } m < 0) \end{cases} - T_{w,n_w} \right) \quad (9)
 \end{aligned}$$

227 Where:

$$\begin{aligned}
 & \int_{(k_w-1)H_w}^{k_w H_w} T_{s,side} dz \\
 228 & Q_{side-loss,k_w} = \frac{\frac{\int_{(k_w-1)H_w}^{k_w H_w} T_{s,side} dz}{\Delta H_w} - T_{w,k_w}}{\frac{1}{h_{side} A_{side,k_w}} + \frac{\delta_{ins,side}}{\lambda_{ins,side} A_{side,k_w}} + \frac{\delta_{con}}{\lambda_{con} A_{side,k_w}} + \frac{\Delta r_{soil}}{2\lambda_{soil} A_{side,k_w}}} \quad (10)
 \end{aligned}$$

$$\begin{aligned}
 & \int_0^{A_p} T_{s,bot} dA_p \\
 229 & Q_{bot,loss} = \frac{\frac{\int_0^{A_p} T_{s,bot} dA_p}{A_p} - T_{w,n_w}}{\frac{1}{h_{bot} A_p} + \frac{\delta_{ins,bot}}{\lambda_{ins,bot} A_p} + \frac{\delta_{con}}{\lambda_{con} A_p} + \frac{\Delta y_{soil}}{2\lambda_{soil} A_p}} \quad (11)
 \end{aligned}$$

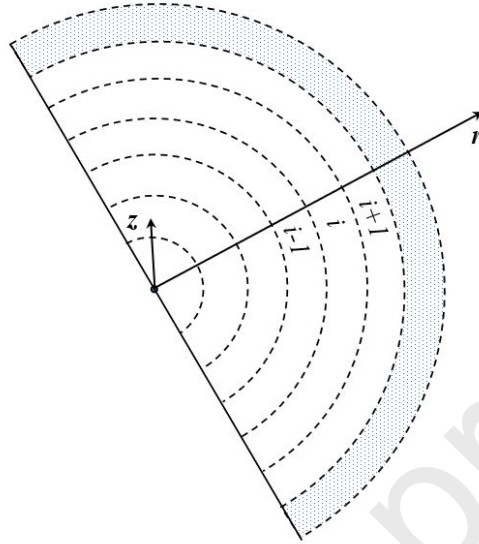
230 When the temperature of the lower water body is higher than that of the upper water body, the following

231 mixing formula shall be followed :

$$232 \quad T_{w,k_w} = T_{w,k_w+1} = \frac{\rho_{w,k_w} V_{w,k_w} T_{w,k_w} + \rho_{w,k_w+1} V_{w,k_w+1} T_{w,k_w+1}}{\rho_{w,k_w} V_{w,k_w} + \rho_{w,k_w+1} V_{w,k_w+1}} \quad (12)$$

233

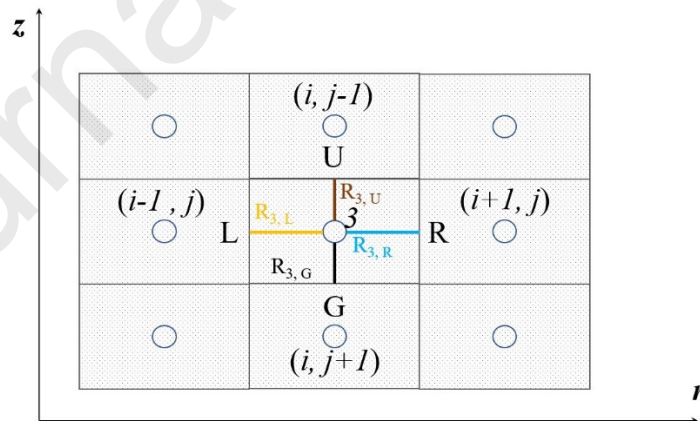
234 In the heat loss of the side and the ground, the weighted average temperature is used at the soil side. It is
 235 worth noting that at this time, the heat transfer at the bottom of the pool should be weighted according to the area,
 236 while the side can be weighted according to the simple length. This is because the heat transfer area of the bottom
 237 node increases with the distance from the column center. See Fig. 5 for details.



238 Fig 5 Schematic diagram of calculated area of the pit bottom
 239

240 2.2.3. Soil region

241 In the heat conduction of the soil region, the temperature of nodes (i, j) in the soil area will depend on the heat
 242 conduction of adjacent nodes, as shown in Fig. 6. Take the heat transfer balance equation of three typical points for
 243 derivation.



244 Fig 6 Typical calculation unit 3 Node (i, j) and its neighbors in soil region
 245
 246

247 Thus, the energy balance for the node 1 in the soil was :

$$248 \quad \rho_{soil} C_{p,soil} V_1 \frac{\partial T_1}{\partial \tau} = \frac{T_L - T_1}{R_{L,R} + R_{1,L}} + \frac{T_G - T_1}{R_{G,U} + R_{1,G}} + \frac{T_{ev} - T_1}{R_{ev} + R_{1,U}} + \frac{\int_0^{\Delta z} T_w dz}{\Delta y} - T_1 + \Delta r I_g \varphi \quad (13)$$

249 Where :

$$250 \quad R_{\sim,U} = R_{\sim,G} = \frac{\Delta z}{2\lambda_{soil}\Delta r} \quad (14)$$

$$251 \quad R_{\sim,L} = R_{\sim,R} = \frac{\Delta r}{2\lambda_{soil}\Delta z} \quad (15)$$

$$252 \quad R_{ev} = \frac{1}{h_{ev}\Delta r} \quad (16)$$

$$253 \quad R_{w,side} = \frac{1}{h_{side}\Delta z} + \frac{\delta_{ins,side}}{\lambda_{ins,side}\Delta z} + \frac{\delta_{con}}{\lambda_{con}\Delta z} \quad (17)$$

254 The energy balance for the node 2 in the soil was :

$$255 \quad \rho_{soil} C_{p,soil} V_2 \frac{\partial T_2}{\partial \tau} = \frac{T_L - T_2}{R_{L,R} + R_{2,L}} + \frac{T_G - T_2}{R_{G,U} + R_{2,G}} + \frac{T_R - T_2}{R_{R,L} + R_{2,R}} + \frac{T_{w,bot} - T_2}{R_{w,bot} + R_{2,U}} \quad (18)$$

256 Where:

$$257 \quad R_{w,bot} = \frac{1}{h_{bot}\Delta r} + \frac{\delta_{ins,bot}}{\lambda_{ins,bot}\Delta r} + \frac{\delta_{con}}{\lambda_{con}\Delta r} \quad (19)$$

258 The energy balance for the node 3 in the soil was :

$$259 \quad \rho_{soil} C_{p,soil} V_3 \frac{\partial T_3}{\partial \tau} = \frac{T_L - T_3}{R_{L,R} + R_{3,L}} + \frac{T_G - T_3}{R_{G,U} + R_{3,G}} + \frac{T_R - T_3}{R_{R,L} + R_{3,R}} + \frac{T_U - T_3}{R_{U,G} + R_{3,U}} \quad (20)$$

260 Semi-infinite and symmetry boundary conditions. The boundary condition at the last node at the semi-infinite
261 boundary in both the radial and axial directions was assumed to be an adiabatic boundary:

$$262 \quad \left. \frac{\partial T}{\partial r} \right|_{r=0} = 0; \left. \frac{\partial T}{\partial r} \right|_{r=Rad} = 0; \left. \frac{\partial T}{\partial z} \right|_{z=0} = 0 \quad (21)$$

263 2.2.4. Solution method

264 In the real operation of the STES coupled with solar system, the energy collected from the sun will be stored
265 in the water of the pit and then passed through a heat exchanger to provide heat to consumers. In this process the

266 heat transfer inside and outside the pit will be coupled. The entire procedure could be expressed by the flowchart of
 267 **Fig. 7.**

268 The hourly air temperature, radiation intensity and wind speed data measured in one year in Hebei are
 269 transferred to the curve and then input into the simulation. The physical properties of each component are shown in

270 **Table 3.** The initial water temperature in the pit is 15 °C, and the initial soil temperature is 10 °C. Basically, for
 271 most numerical models, such as the finite difference method, appropriate time steps must be given to ensure the
 272 stable calculation of unsteady heat transfer problems. Larger time step can accelerate any type of simulation model,
 273 but it will also lead to unreasonable results of some numerical models. In order to test the robustness of the model,
 274 the typical energy release stage of the Huangdicheng project is used to test the operation of the **Stes STES** with
 275 different time steps.

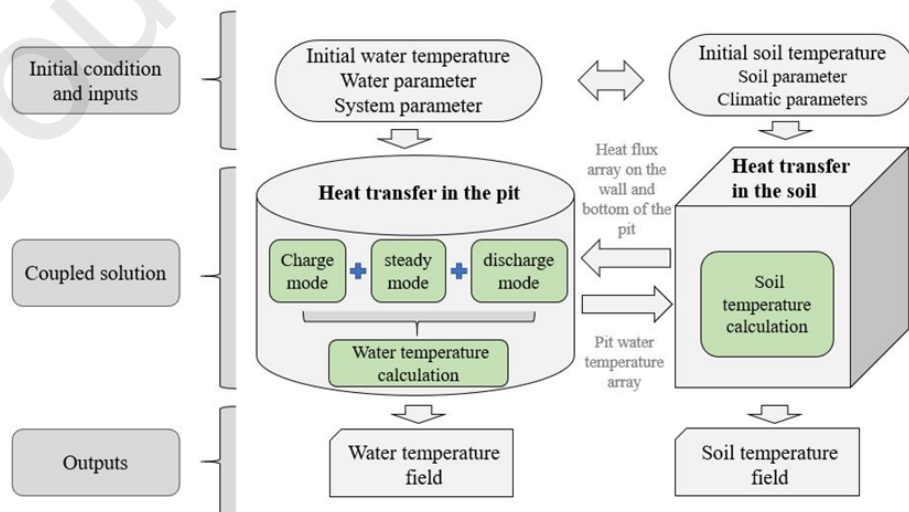
276 **Table 3**

277 Thermal physical properties of the material in the experiment.

Material	Geometric dimension(m)	Density(kg/m ³)	Thermal conductivity(W/m/°C)	Specific heat(J/kg/°C)
Cover plant	0.3	28	0.042	1500
Air	0.3	1.12	0.023	1005
Water	~	980	0.69	4195
Concrete	0.3	2500	1.74	970
Soil	~	1400	3.15	1600

278

279 **Fig. 8** shows the comparison results between the numerical solution and the measured data of the project. As
 280 shown in **Fig. 8**, the time steps of 60s, 360s, 600s, 3600s and 6000s are used in the STES model, and the temperature
 281 scatter points almost overlap. In the discharging stage, the error decreases gradually with the increase of time. The
 282 reason is that there is some gap between the initial soil boundary conditions and the experiment. With the increase
 283 of time, the soil boundary tends to be stable and closer to the measured data. The overall results prove the robustness
 284 of the model and the effectiveness of long-term simulation of STES with large time step in order to improve the
 285 simulation efficiency. Based on this result and model robustness proof, in the long-term analysis and Simulation of
 286 STES, in order to save time, the time step is set to 1 hour, which is suitable for the requirements of section 3 and
 287 section 4.

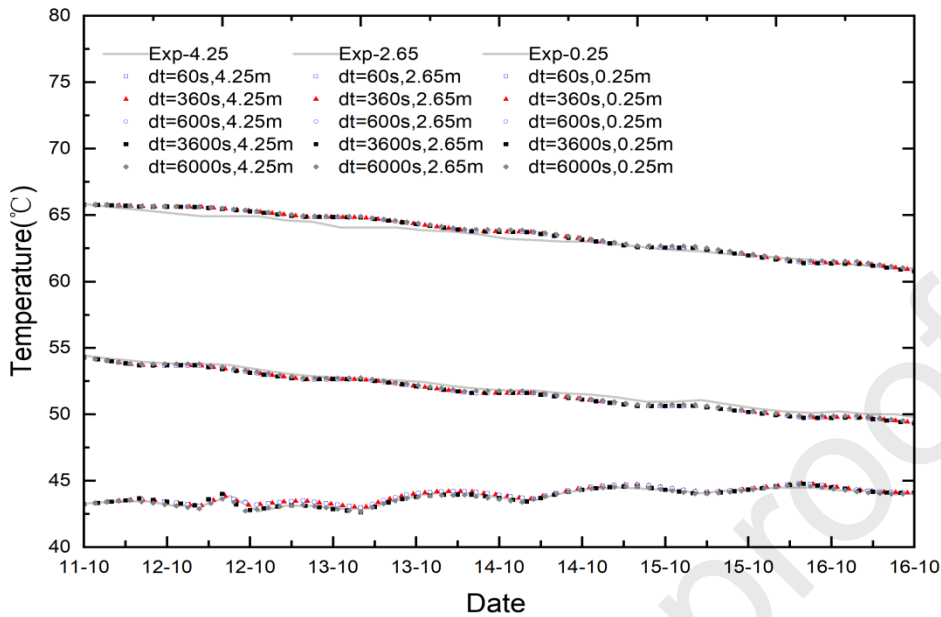


288

289

Fig 7 Modeling process and internal logical of numerical model for STES

290



291

292

Fig 8 Comparing simulation results of STES with experimental results

293

3. Model verification

294

In order to verify the validity and accuracy of the proposed model, the operation data of Huangdicheng project are used for verification. In the Huangdicheng project, the temperature measuring points of the water are located at the height of 4.25m, 2.65m and 0.25m from the bottom of the pit. In typical charge days and typical discharge days, there are standby conditions, so typical standby does not do specific verification. The initial water temperature of each layer was calculated by curve fitting with the in-route data points. The charging and discharging flow and temperature were collected by the data points in the figure. The meteorological conditions were based on the weather data files of the same period. On typical charging days (June 1, 2018 to June 8, 2018) the results are shown in the figure.

302

On a typical discharging mode day (October 11, 2018 to October 16, 2018) the results are shown in the figure below.

304

In the simulation, a time step of 60s was used to compare the water temperature of each time step with the measured curve through the simulation of 168h in the charging stage and 120h in the discharging stage of the model. The results are shown in Fig. 9-8 & Fig. 10-9. The simulation results are in good agreement with the measured ones. The analysis shows that the average relative error of the charging model is only 1.57%, and the average error temperature is 0.44°C. The average relative error of the discharging model is only 0.46%, and the average error

308

309

temperature is 0.24°C. Simulation errors come from two aspects : (1) the system parameters used in the model may be different from the actual situation; (2) For the convenience of calculation, the water heat transfer model adopts the quasi-dynamic model, assuming that the physical properties are unchanged. Considering the small simulation error, this model can accurately describe the water temperature change in STES.

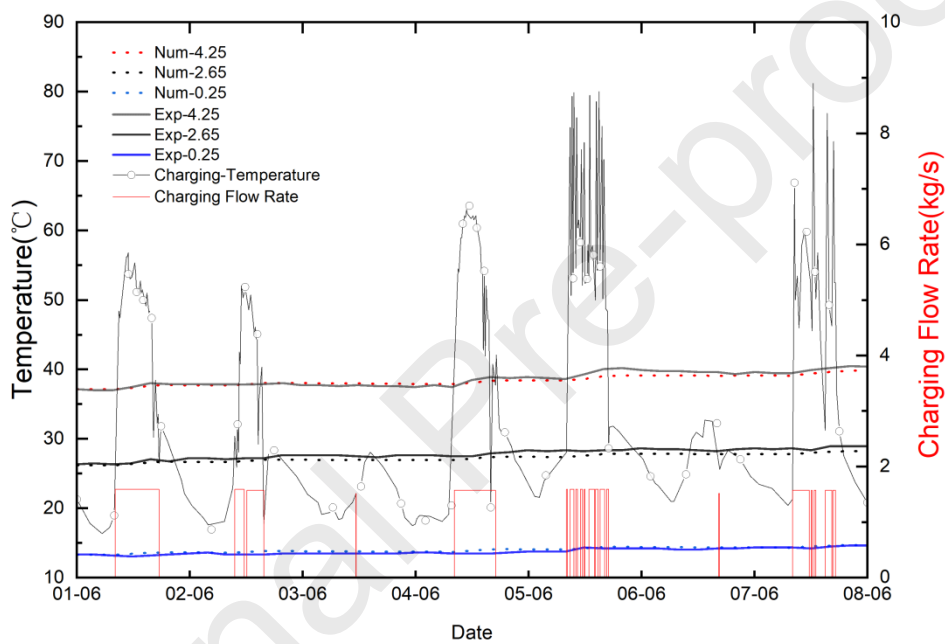
310

311

312

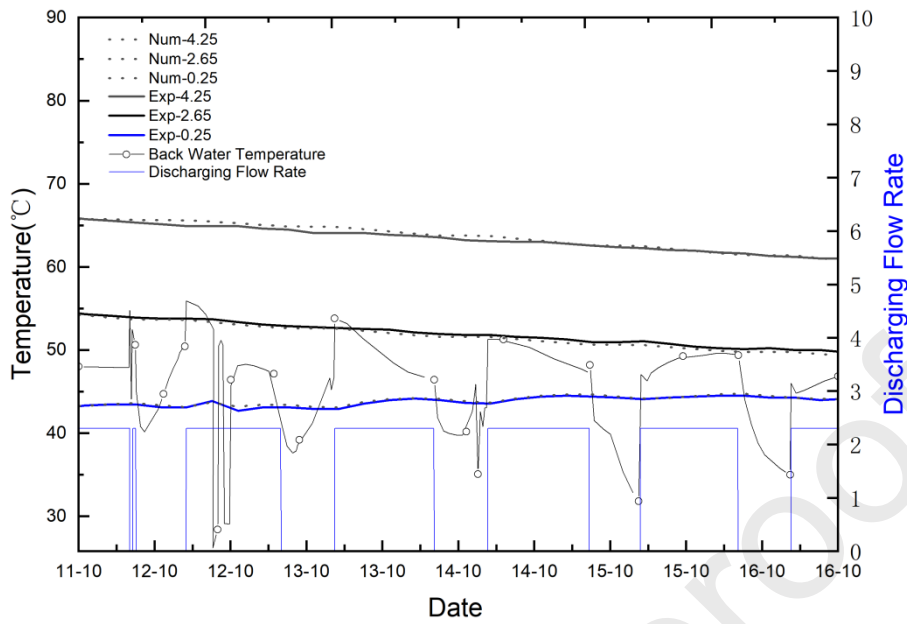
313 **Fig. 10** shows the comparison results between the numerical solution and the measured data of the project. As
 314 shown in Fig. 8, the time steps of 60s, 360s, 600s, 3600s and 6000s are used in the STES model, and the temperature
 315 scatter points almost overlap. In the discharging stage, the error decreases gradually with the increase of time. The
 316 reason is that there is some gap between the initial soil boundary conditions and the experiment. With the increase
 317 of time, the soil boundary tends to be stable and closer to the measured data. The overall results prove the robustness
 318 of the model and the effectiveness of long-term simulation of STES with large time step in order to improve the
 319 simulation efficiency. Based on this result and model robustness proof, in the long-term analysis and Simulation of
 320 STES, in order to save time, the time step is set to 1 hour, which is suitable for the requirements of section 3 and
 321 section4.

322
 323
 324



325
 326
 327
 328
 329

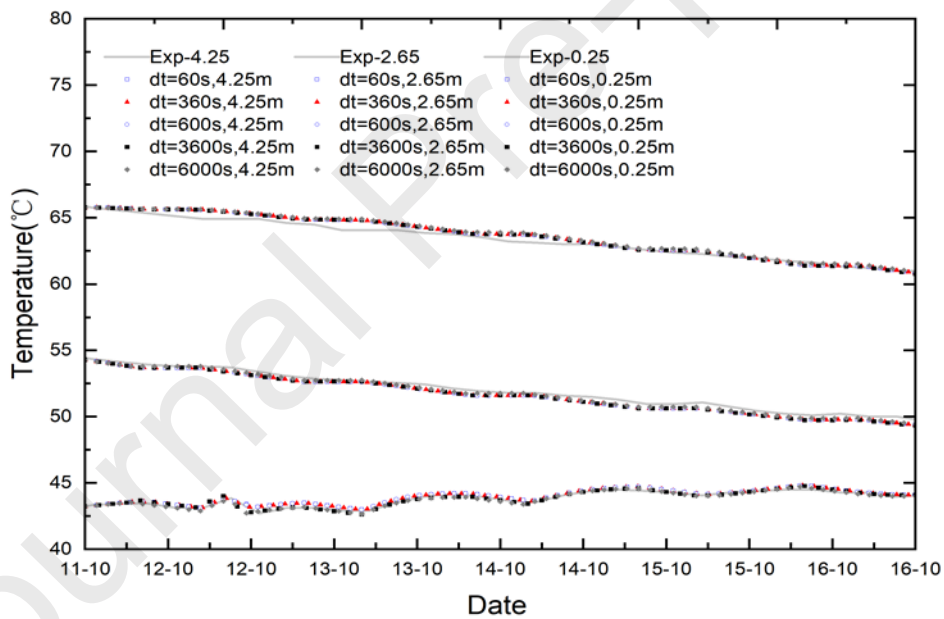
Fig 9-8 Temperatures in the water pit during the typical charging mode days[13]



330

331

Fig 10-9 Temperatures in the water pit during the typical discharging mode days[13]



332

333

Fig 8-10 Comparing simulation results of STES with experimental results

334

4. Analysis and discussion

335

336

337

338

In order to verify the influence of climate environment on STES, the data input of temperature, wind speed and radiation in Baoding city of Hebei Province in 2005 were selected to conduct simulation calculation. Baoding city belongs to the central heating region of north China, and is located in the plain adjacent to the metropolis, so it is appropriate to build STES district heating system here.

339 4.1. Energy balance

340 4.1.1 Definitions

341 Heat loss at the top, sides and bottom is calculated using temperature data within each time step.

342 The heat loss from the top was calculated as:

$$343 \quad Q_{top,loss} = \sum_{k_i=1}^{n_i} \frac{T_{ev} - T_{w,1}}{\frac{\partial_a}{\lambda_a} + \frac{\Delta H_w}{2\lambda_w} + \frac{1}{h_{ev}}} A_p \quad (22)$$

344 The heat loss from the side wall was calculated as:

$$345 \quad Q_{side,loss} = \sum_{k_i=1}^{n_i} \sum_{k_w=1}^{n_w} \frac{\int_0^{k_w H_w} T_{s,side} dy}{\frac{1}{h_{side,k}} + \frac{\partial_{ins,side}}{\lambda_{ins,side}} + \frac{\partial_{con}}{\lambda_{con}} + \frac{\Delta r}{2\lambda_s}} A_{side,k} \quad (23)$$

346 Here, k_w is the number of the nodes in the water region and k_i is the number of the nodes in the timing.

347 The heat loss from the bottom was calculated as:

$$348 \quad Q_{bot,loss} = \sum_{k_i=1}^{n_i} \frac{\int_0^{A_p} T_{s,bot} dA_p}{\frac{1}{h_{bot}} + \frac{\partial_{ins,bot}}{\lambda_{ins,bot}} + \frac{\partial_{con}}{\lambda_{con}} + \frac{\Delta r}{2\lambda_s}} A_p \quad (24)$$

349 The total heat loss from the water pit was then:

$$350 \quad Q_{total-loss} = Q_{top,loss} + Q_{side,loss} + Q_{bot,loss} \quad (25)$$

351 Here, Q_{ch} is the energy input into the water pit during charging mode, which was calculated as:

$$352 \quad Q_{ch} = \rho_w C_{p,w} \sum_{k_i=1}^{t_{ch}} m_{in} (T_{out,co} - T_{in,co}) \quad (26)$$

353 Q_{disc} is the energy discharged from the water pit during discharging mode, which was calculated as:

$$354 \quad Q_{disc} = \rho_w C_{p,w} \sum_{k_i=t_{ch}+1}^{t_{ch}+t_{disc}} m_{out} (T_{in,disc} - T_{out,disc}) \quad (27)$$

355 ΔQ is the internal energy change in the water pit, which was calculated as:

$$356 \quad \Delta Q = \rho_w C_{p,w} \sum_{k_w=1}^{n_w} (T_{w,k_w} - T_{ini,k_w}) A_p \Delta H_w \quad (28)$$

357 Then, the water pit storage efficiency was defined as:

$$358 \quad \eta = \frac{Q_{disc} + \Delta Q}{Q_{ch}} \quad (29)$$

359 4.1.2 energy flow

360 In the initial setting of the system, the water temperature is 15°C, the soil temperature is 10°C, and the time step
 361 is 3600s. The point data were selected from the fitting curve of the annual temperature, radiation intensity and wind
 362 speed meteorological data of Hebei province in 2015. The initial operation time of the system's energy charging
 363 mode was set as April 1 after the end of northern heating, and the initial operation time of the energy discharge mode
 364 was set as November 15.

365 In the whole year operation of the system, the charging time is 225 days and the discharging time is 135 days.
 366 In the system charging condition, when the collector cannot heat the inlet water temperature of the collector, or the
 367 irradiation is zero, the system is in the standby condition, and vice versa. In the release of energy, the use of 10°C
 368 temperature difference heating, from 16.00 p.m. every day to the next morning 8.00 operation, the whole day running
 369 for 16 hours. The specific data is plotted as follows:

370

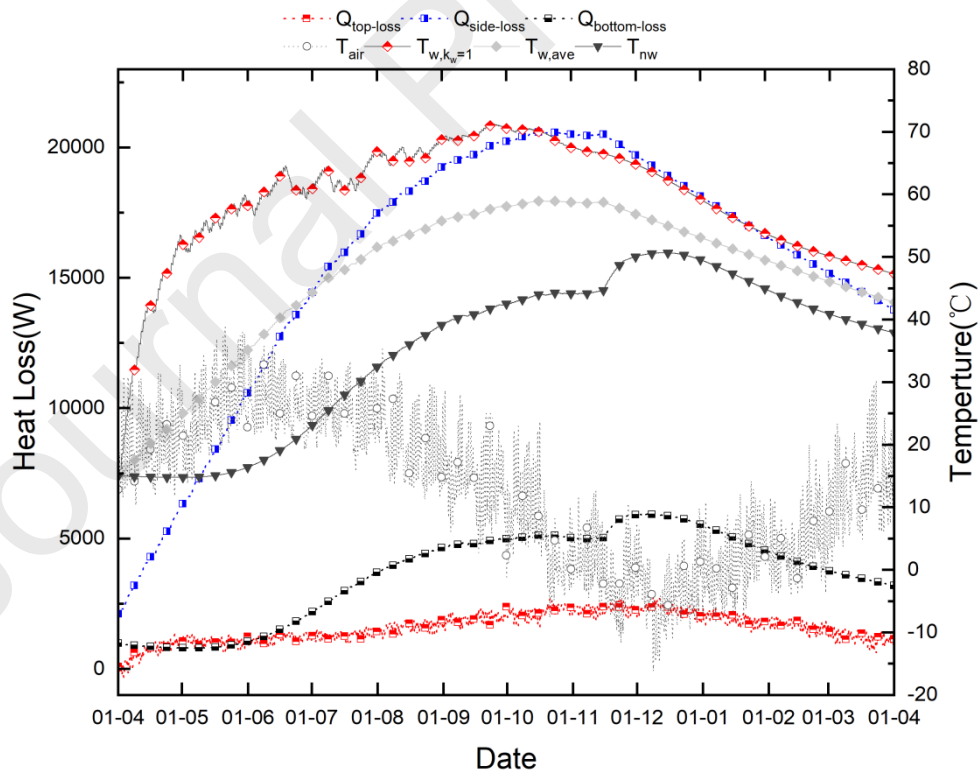
371

Table 2

372

The energy change of the water pit

	Total-Loss	Total-Rise	Total-Out	Total-In	η
Total (MWh)	180	358	145	683	--
Fraction (%)	26.35	52.42	21.23	100	73.65



373

Fig 7 Hourly heat loss diagram of the pit

374

375

Table 3

376

Energy loss of the water pit

	Top	Side	Bottom	Total
Total (MWh)	13.91	134.44	31.74	180.09
Fraction (%)	7.73	74.65	17.62	100

377

Table 4 shows that in a complete operation cycle from 1st Day of the first year to 1st day of the second year, the solar collector system is charged with a total energy of 683MWh, of which the energy discharge is 145MWh, accounting for 21.23%; Water internal energy increased by 358MWh, accounting for 52.42%; The total heat loss through the top, side and bottom is 180MWh, accounting for 26.35%. System efficiency in the first year is 73.65%, which is slightly higher than the reported value of Hannover 3000 m³ pool (71.2%)[22].

382

383

384

385

386

387

388

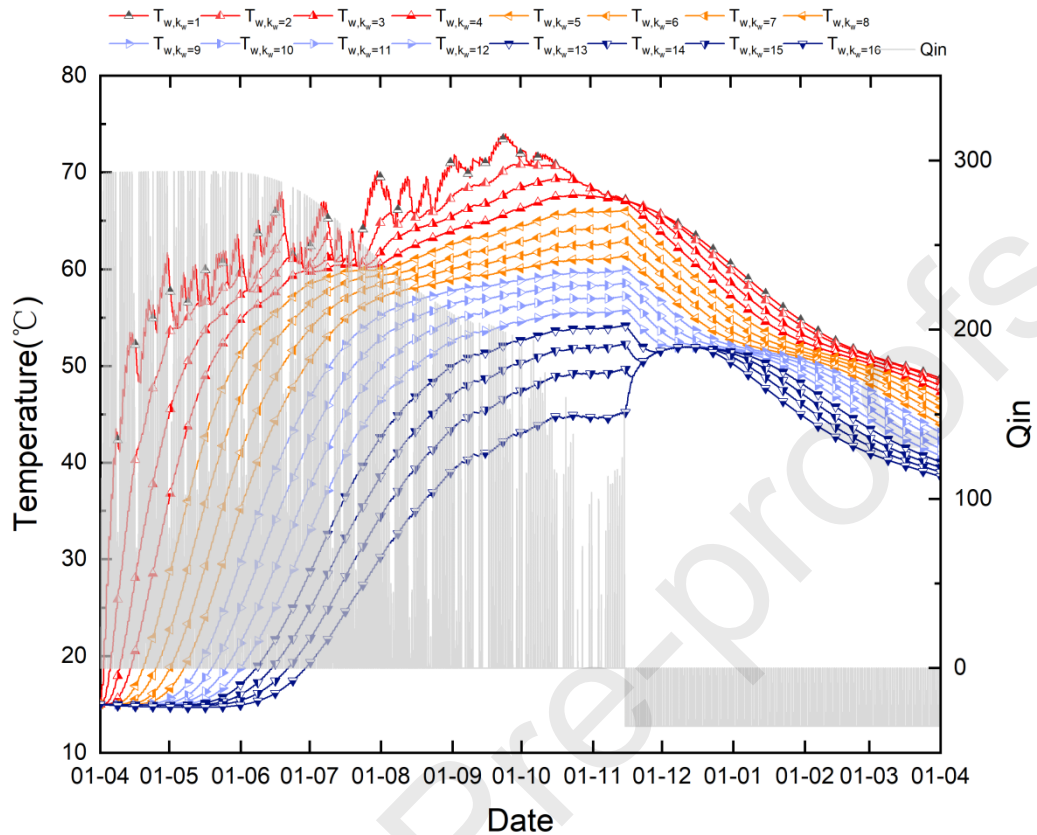
389

390

Fig. 11 shows the top, side and bottom heat loss of the pit over time. As can be seen from the figure, The change of $Q_{top-loss}$ is mainly related to the temperature difference between the topmost water and the environment; $Q_{side-loss}$ is mainly linearly related to the average temperature of the water; And $Q_{bottom-loss}$ is mainly linearly related to the temperature of the bottom water. At the beginning, $Q_{top-loss}$ is less than zero because the initial water temperature is lower than the ambient temperature. Among all heat losses of the pit, the top heat loss is 13.91MWh, accounting for 7.73%. This is because the top has a well-insulated air layer, which makes the top account for the smallest heat loss. The total heat loss at the bottom is 31.74MWh, accounting for 17.62% of the total heat loss, because the bottom temperature is low throughout the operation stage. The side heat loss reached 134.44, accounting for 73.65%, which is the largest part of the entire system heat dissipation.

391

4.1.3 Temperature change



392

393

Fig 8 Time-by-hour change of the water temperature in each layer of the pit

394

During operation, the water body is evenly divided into 16 layers, and the temperature changes of each layer are shown in **Fig. 12**. In the charging stage, the highest temperature of the water was the temperature of the first

395

layer of water on September 23, and the temperature was 74.05°C. At the end of charging, the maximum temperature

396

397

of the water is 67.20°C, the minimum temperature is 45.23°C, and the average water temperature is 58.74°C. After

398

the discharging state, the maximum temperature of the water is 48.72°C, the minimum temperature is 38.52°C, and

399

the average temperature is 43.63°C.

400

During the charging phase, the temperature of the upper water body sometimes decreases because the total heat charged is less than the total heat loss (including heat transfer between water bodies) at the same time. The charging energy decreases with the rise of the bottom temperature. In the later period, due to the high bottom temperature and the end of summer, the solar radiation intensity is insufficient, so the charging energy decreases rapidly after the start of October 1.

404

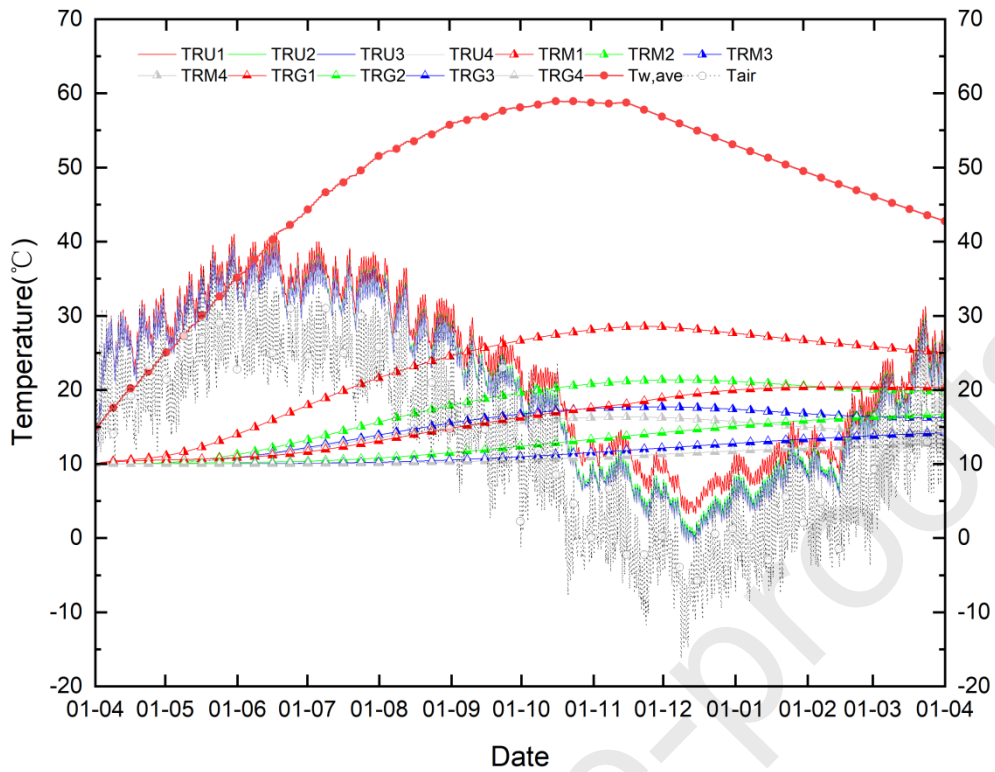
405

In the discharging stage, because the temperature difference of 10°C is used for heating, the temperature of the water body flowing into the system is higher than the temperature of the bottom water body, which soon causes the mixing of the lower water body. With the passage of time, the temperature of the influent water body decreases, and the thermal stratification between the water layers tends to be stable.

406

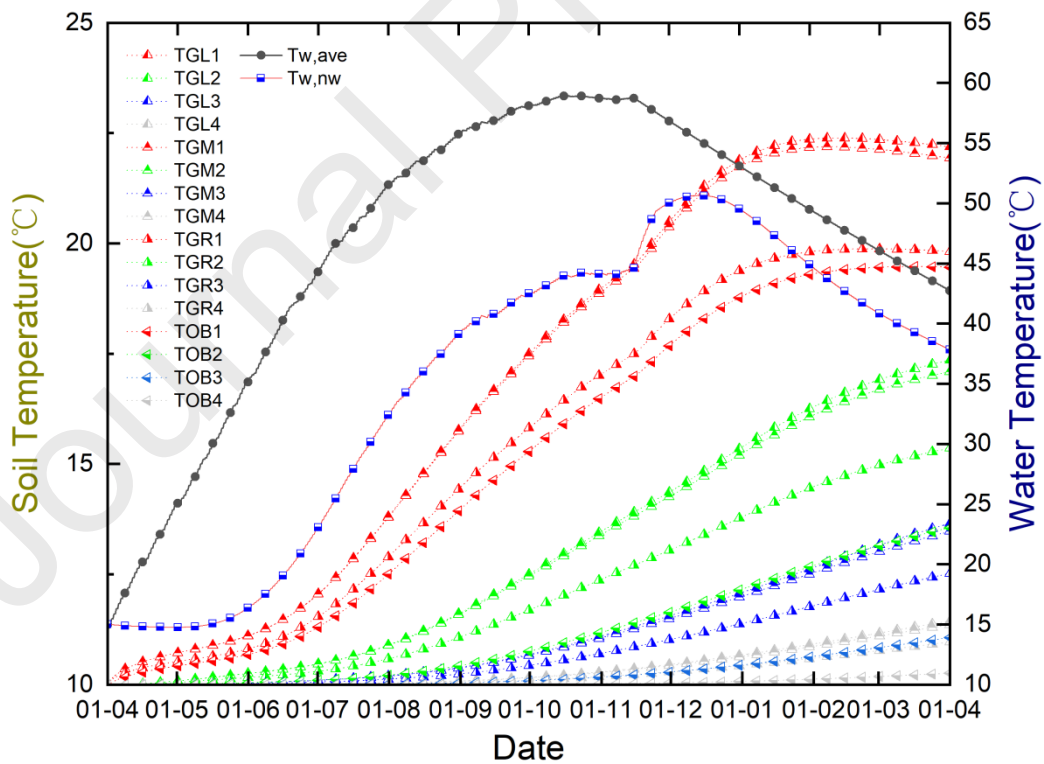
407

408



409
410

Fig 9 Soil temperature changes on the side of the pit



411
412

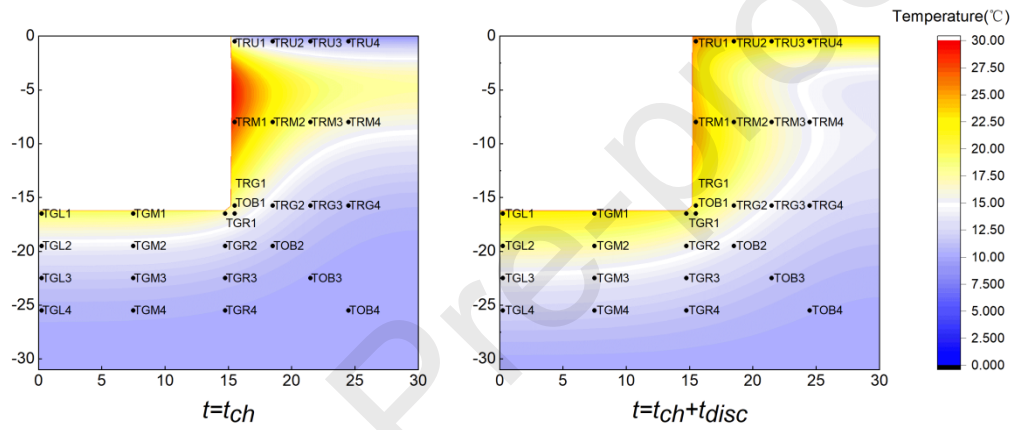
Fig 10 Soil temperature changes at the bottom of the pit

413 **Fig. 13** shows the temperature change of the soil measurement points on the side of the pit. Generally speaking,
414 the temperature measuring points on the top layer are linearly related to the ambient air temperature because the

415 depth of the buried soil is shallow, but generally slightly higher than the air temperature. It's because of the heat
 416 transfer from the pit. The soil temperature within 12m close to the pool wall has a high correlation with the average
 417 temperature in the pool, but as the distance increases, there will be an obvious phase difference between the two. It
 418 can also be seen in **Fig. 13** that the temperature measurement points of TRM1, TRM2 and TRM3 are not highly
 419 correlated with the air temperature change, which indicates that the influence of meteorological factors on the soil
 420 is about 8m in the one-year operation cycle.

421 **Fig. 14** shows the temperature change of the soil measurement points at the bottom and obliquely below of the
 422 pit. Because the water temperature at the bottom of the pit is higher than the soil temperature all the time, the soil
 423 temperature in this area has been increasing in the early stage. When the water temperature at the bottom of the pit
 424 drops, the soil temperature within 5m close to the bottom of the pit will also slowly drop, but the soil temperature in
 425 further areas will slowly rise.

426 **Fig. 15** shows the cloud diagram of soil temperature distribution at the end of charging stage and the whole
 427 cycle. With the extension of running time, the thermal influence radius of the pool expands.



428
429
430 **Fig 11** Soil temperature distribution after charging and discharging stage
431

432 4.1.4. Stratification number and MIX number

433 The stratification number and the MIX number have both been used to evaluate the thermal stratification in the
 434 water pit of STES.

435 The stratification number is defined as the ratio of the mean temperature gradient in the water pit to the
 436 maximum mean temperature gradient in the water pit during the test period[29]:
 437

$$438 \text{Str}(\tau) = \frac{\overline{(\partial T / \partial y)_{\tau}}}{(\partial T / \partial y)_{max}} \quad (30)$$

439 The average derivative is given by:

$$440 \overline{(\partial T / \partial y)_{\tau}} = \frac{1}{n_w} \left[\sum_{k=1}^{n_w-1} \left(\frac{T_{w,k+1} - T_{w,k}}{\Delta H_w} \right) \right] \quad (31)$$

441 During the entire operation, the maximum mean temperature gradient is:

$$442 \quad \overline{(\partial T / \partial y)}_{max} = \frac{1}{n_w} \frac{T_{w,max} - T_{w,min}}{\Delta H_w} \quad (32)$$

443 Where $T_{w,max}$ and $T_{w,min}$ are the maximum and minimum water temperatures during the entire operation.

444 The MIX number is useful for evaluating the thermal stratification in a water pit at a specific time and ranges
445 from 0 to 1 which reflects the degree of stratification independent of the working conditions[30].

$$446 \quad MIX = \frac{Mp_{stratified} - Mp_{exp}}{Mp_{stratified} - Mp_{full-mixed}} \quad (33)$$

447 Where Mp_{exp} is the amount of internal energy in the pit water under the simulation situation, and its
448 calculation formula is as follows:

$$449 \quad Mp_{exp} = \sum_{kw=1}^{n_w} H_{kw} \cdot E_{kw} \quad (34)$$

$$450 \quad E_{kw} = \rho_{w,kw} V_{kw} C_{p,w} T_{w,kw} \quad (35)$$

451 The energy content of a perfectly stratified tank is assumed to be the same as that of the experimental water pit

452 In the perfectly stratified tank, the thermal stratification of the pit water is composed of two layers, and the
453 temperature of the two layers of water body is the highest and lowest temperature in the simulation experiment at
454 the same time.

$$455 \quad E_{stratified} = E_{exp} = E_{stratified,hot} + E_{stratified,cold} \quad (36)$$

$$456 \quad \rho_w C_{p,w} V_{hot} T_{hot} + \rho_w C_{p,w} V_{cold} T_{cold} = E_{stratified} \quad (37)$$

$$457 \quad V = V_{hot} + V_{cold} \quad (38)$$

$$458 \quad V_{cold} = \pi R^2 H_{stratified} \quad (39)$$

$$459 \quad Mp_{stratified} = \frac{H + H_{stratified}}{2} E_{stratified,hot} + \frac{H_{stratified}}{2} E_{stratified,cold} \quad (40)$$

460 The energy content in a fully mixed tank is also assumed to be equal to the energy content in an experiment
461 tank, and its calculation formula is as follows:

$$462 \quad E_{full-mixed} = E_{exp} \quad (41)$$

$$463 \quad Mp_{full-mixed} = \frac{HE_{full-mixed}}{2} \quad (42)$$

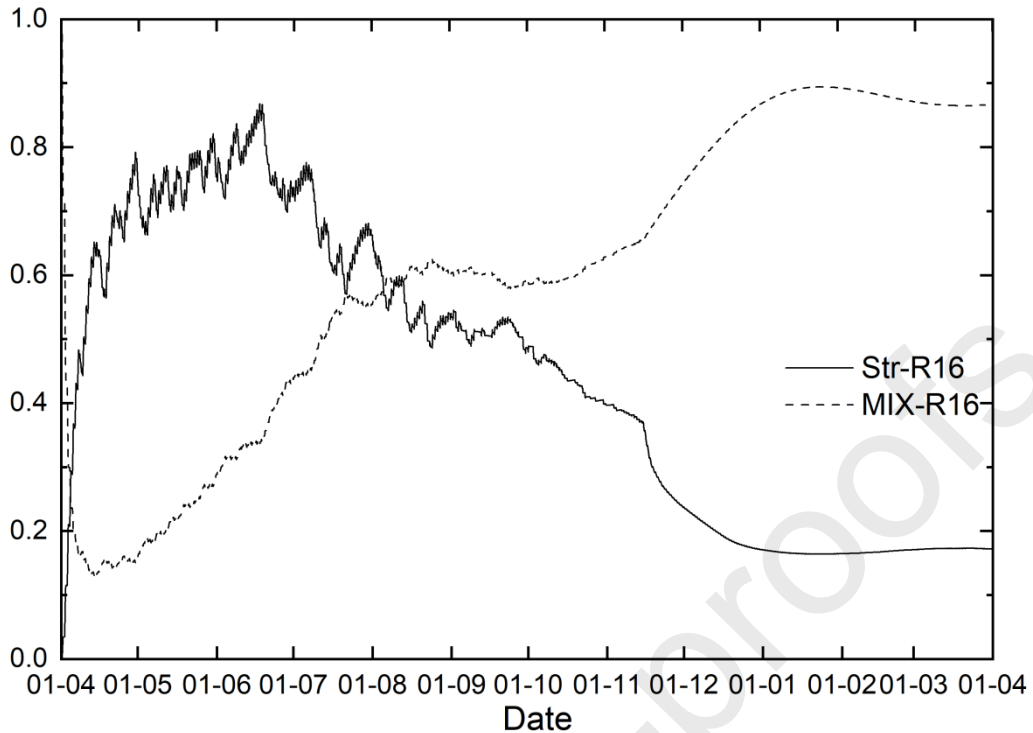


Fig 16 Variation of stratification number and MIX number of water body in water pit

Due to the initial uniform temperature distribution of the water pit, the stratification number is equal to zero at the beginning, as shown in **Fig. 16**. Then, the solar collector will gradually charge the pool, so between April 1 and June 17, the stratification number increases from 0 to the peak value of 0.87. The stratification number is close to the report of Fernandez et al[29]. From June 17 to November 15, the stratification number gradually decreased from 0.87 to 0.37, indicating that the mixing increased during the charging process. In this case, it is likely that the charging energy decreased and the temperature of the upper layer water decreased, resulting in the mixing between the upper water.

In the discharging phase, from November 15 to April 1 of the next year, the stratification number decreased from 0.37 to 0.17, and then gradually stabilized.

During the whole operation period, the variation trend of stratification number and MIX number is almost opposite, with the decrease of stratification number and the increase of MIX number, both of which reflect the decrease of thermal stratification of water body.

4.2. Impact of different depth diameter ratio

4.2.1 Definitions

In reality, the volume of STES is often planned according to the total load of the heating area, so it is necessary to keep the volume of STES unchanged and change the depth-diameter ratio to explore its heat storage characteristics.

In this model, the depth of the initial pit is $H=16\text{m}$, the diameter is $D=30\text{m}$, and the total volume of the pit is 11304m^3 . Under the condition that the model change keeps the volume as close to 11304m^3 as possible, the following 6 Models are set as **Table. 6**.

486

487

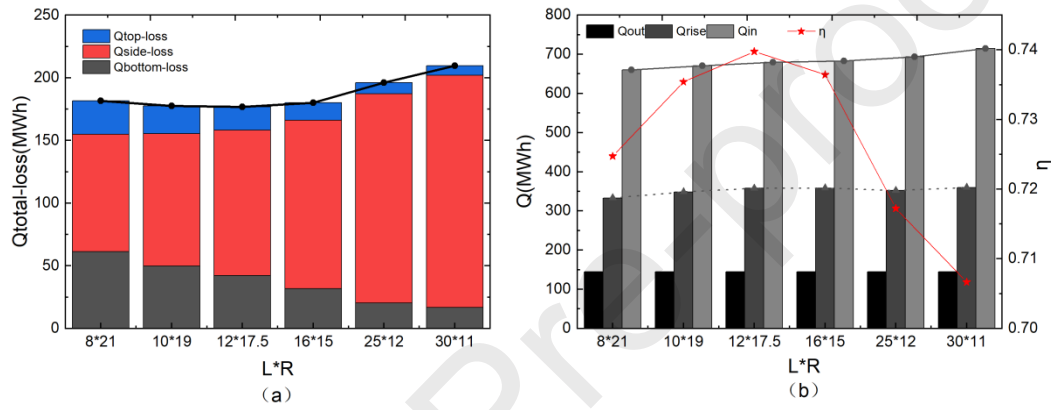
Table 4

488

Parameters of different depth diameter ratio

	Model1	Model 2	Model 3	Model 4	Model 5	Model 6
Height, H (m)	8	10	12	16	25	30
Diameter, D (m)	42	38	35	30	24	22
Area, A (m ²)	3824	3460	3242	2920	2788	2832
Volume, V (m ³)	11077	11335	11539	11304	11304	11398
H/D (-)	0.19	0.263	0.343	0.533	1.042	1.364
A/V (1/m)	0.345	0.305	0.281	0.258	0.247	0.249

489



490

491

Fig 17 Comparison of heat loss with different depth-diameter ratio

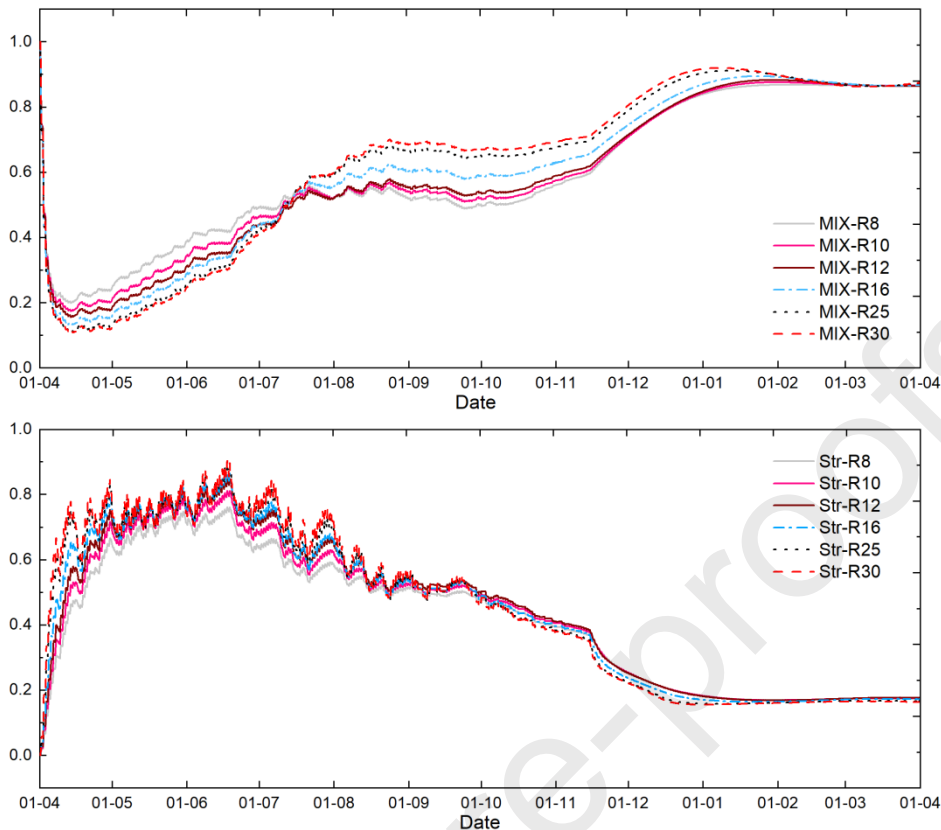


Fig 18 Variation of stratification number and MIX number of different cases

492

493

494

495 As can be seen from Fig. 17, with the increase of the depth-diameter ratio, the total heat loss tends to decrease
 496 first and then increase, that is, there is an optimal depth-diameter ratio. In the small depth-diameter ratio model, the
 497 total and ratio of heat loss at the top and bottom of the pit are relatively large, because the smaller depth-diameter
 498 ratio means that the heat transfer area at the top and bottom is larger, and the smaller depth-diameter ratio also means
 499 that the thermal stratification of the water is reduced and the temperature of the water at the bottom of the pit is
 500 higher, which also increases the heat dissipation at the bottom. In Model1, the heat loss at the top and bottom
 501 accounts for 48.5% of the total heat loss of the model.

502 In the larger depth-diameter ratio, the proportion of side heat loss increases. In Model6, the side heat loss
 503 accounts for 88.3% of the total heat loss of the model.

504 As shown in Fig. 17, in models with different depth-diameter ratios, the total internal energy of water does not
 505 change much, but with the increase of depth-diameter ratio, the total energy charged will also increase. This is
 506 because a higher depth-diameter ratio means a lower bottom temperature, which is conducive to improving the
 507 efficiency of solar collector. As shown, the relatively optimal value of H/D in this simulation is around 0.343. At
 508 this ratio, the system efficiency reaches the highest 74% of the models. When the depth-diameter ratio exceeds this
 509 value, the system efficiency will drop sharply as the aspect ratio increases.

510 It can be seen from Fig. 18 that Model3 has a relatively low MIX number and a relatively high Stratification
 511 number, which indicates that a reasonable thermal stratification phenomenon is conducive to improving the operating
 512 efficiency of the STES system, but this is not absolute.

513 4.3. Influence of discharge mode on system efficiency in the coming year

514 4.3.1 Definitions

515 After the first operating cycle, the relative internal energy (water temperature) of the STES system will
 516 significantly affect the operating efficiency of the system in the second year. So, the next step is to discuss the
 517 changes of system operating conditions under different energy discharge modes by using 6 Cases from three aspects:
 518 flow rate, daily operating time, and heating temperature difference. The specific parameter settings are shown in
 519 **Table 7**, and in the discharging stage, the temperature change curve of water in different cases and the hourly
 520 charging scatter diagram of the collector are given in Appendix A-

521

522

523

524

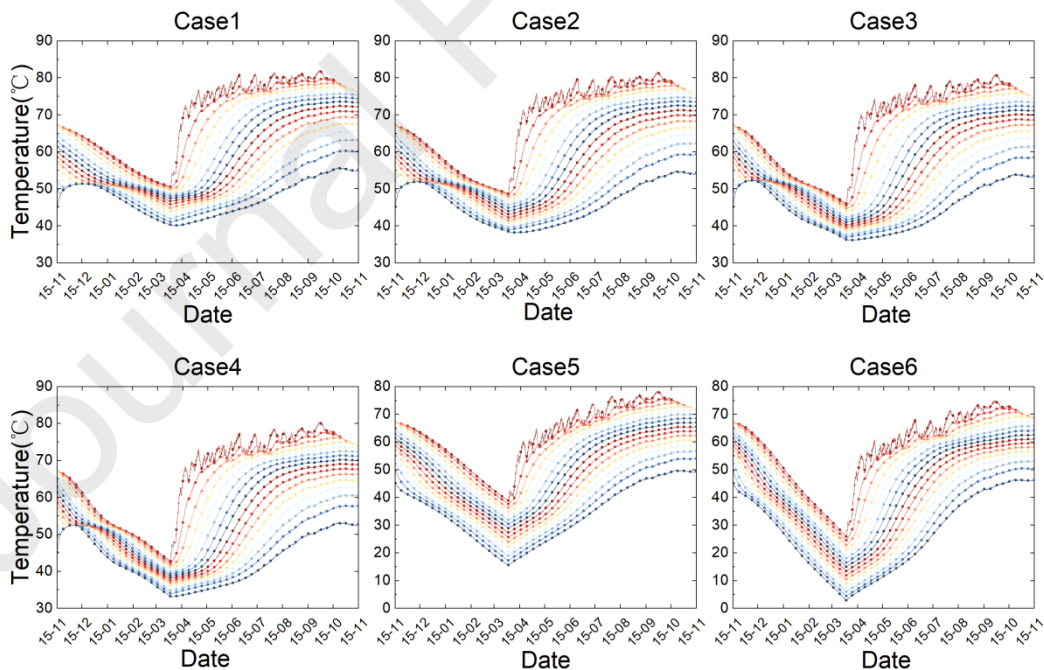
525

Table 5

526

System operating parameters under different energy discharge modes

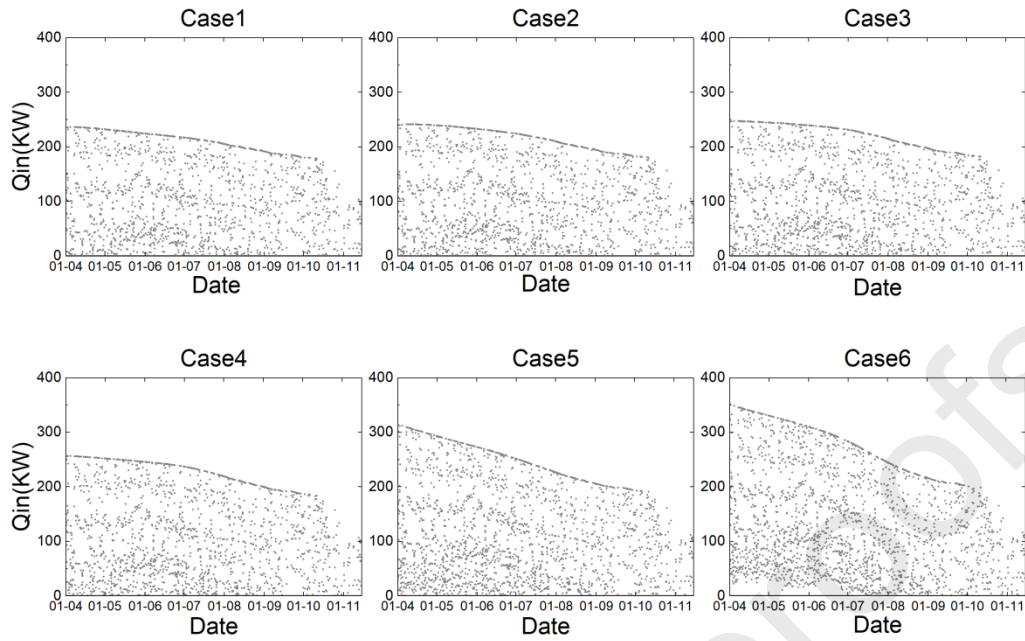
	Case1	Case2	Case3	Case4	Case5	Case6
Flowrate (kg/s)	0.82*0.75	0.82	0.82*1.25	0.82	0.82	0.82
Run_time/D (h)	16	16	16	24	16	24
TD (°C)	10	10	10	10	25	25



527

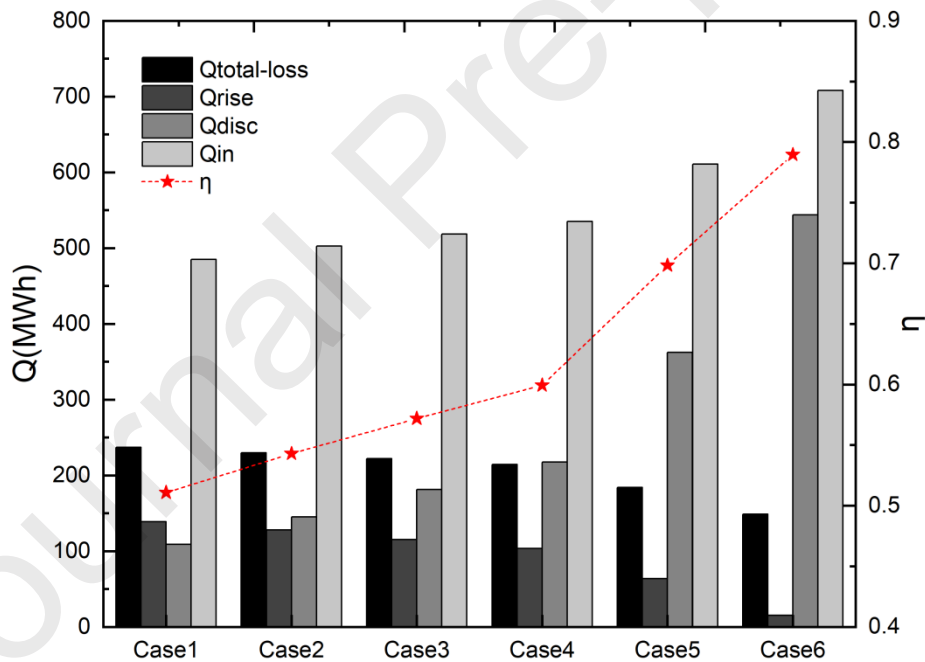
528

Fig 19 Changes in the temperature of the water in the pit under different energy discharge cases



529
530

Fig 20 Changes in the energy charged into the pit in the second year under different energy discharge cases



531
532
533

Fig 21-19 Energy flow of the pool under different energy discharge modes

534
535
536
537
538
539

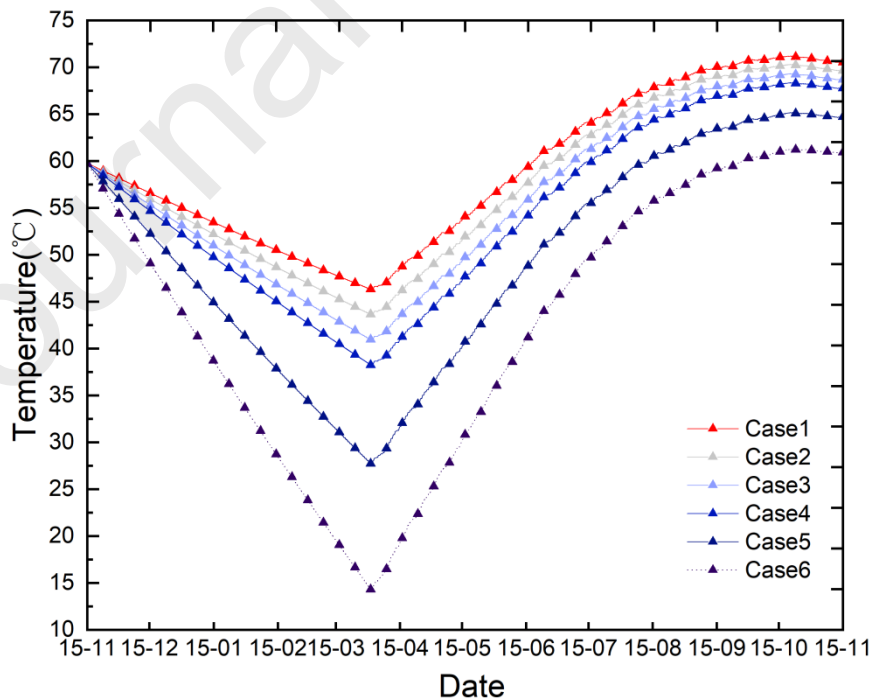
It can be seen from **Case5** and **Case6** in **Fig.A-1** in the appendix **Fig. 19** that in the discharging stage, when a large temperature difference is used for heating, the mixing phenomenon of the bottom water of the pit almost disappears, but the large temperature difference and no mixing means that the water layers are not mixed. Mixing is reduced, the temperature gradient is larger, and increasing the heating time can effectively reduce the temperature gradient between the water layers. In the second charging stage, if the residual temperature of the water has a higher temperature gradient, it means a smaller charging energy at this stage, as shown by **Case5** and **Case6** in **Fig. 20A-2**

540 [in the appendix](#). This is because the higher temperature gradient in the residual temperature means that the
 541 temperature of the bottom water differs greatly from the temperature of the upper layer water. When the charging
 542 starts, the upper layer water is charged into the lower layer, and the temperature of the lower layer will rise faster. A
 543 rapidly rising bottom water temperature will cause the solar collector efficiency to drop faster, so that less heat will
 544 be charged into the uppermost water than in a model with a slower rising bottom temperature. Such slowness and
 545 quickness between the top and bottom water temperatures will result in a larger initial temperature gradient, which
 546 means a smaller water layer temperature gradient during the second charge.

547 However, it is worth noting that in **Case 6** in [Fig. 19A-1](#), the temperature of the upper water body is only
 548 slightly higher than 25°C, while the temperature of the bottom layer is only about 3°C. If 25°C is used for heating,
 549 the return water temperature will be 0°C. There are still some differences from the actual situation.

550 [Fig. 20 A-2](#) shows the hourly charging energy of the solar collector under the 6 Cases, and the lower bottom
 551 temperature can indeed increase the efficiency of the solar collector, thereby increasing the charging energy.
 552 However, this is also related to the initial temperature gradient between the water layers. With a higher temperature
 553 gradient, the temperature of the bottom water body will rise faster, and the efficiency of the solar collector will also
 554 decrease significantly. On the premise of increasing the heating temperature difference to reduce the residual
 555 temperature of the bottom water, the method of increasing the heating time can be used to reduce the temperature
 556 gradient between the water layers.

557 [Fig.-2119](#) shows the energy variation relationship between different discharge cases. Obviously, higher water
 558 residual temperature after the first discharge means that the efficiency of charging in the second year will decline
 559 sharply. There are two main reasons for this situation: first, higher residual temperature of water means that water
 560 will increase its external heat loss; second, higher residual temperature of the water will reduce the efficiency of
 561 solar collector during charging in the second year, thus reducing the total charged energy. This can also be proved
 562 in [Fig. 2220](#). The average temperature difference between **Case1** and **Case6** was 32°C after the end of the first stage



563 of energy discharge, but it increased to 10°C after the end of the second stage of charging.

564

565

Fig 22-20 Variation of average temperature of the water under different discharging energy cases

566

567

4.4. Discussion on the first charging operation

568

569

570

571

572

573

574

575

576

577

578

579

580

581

582

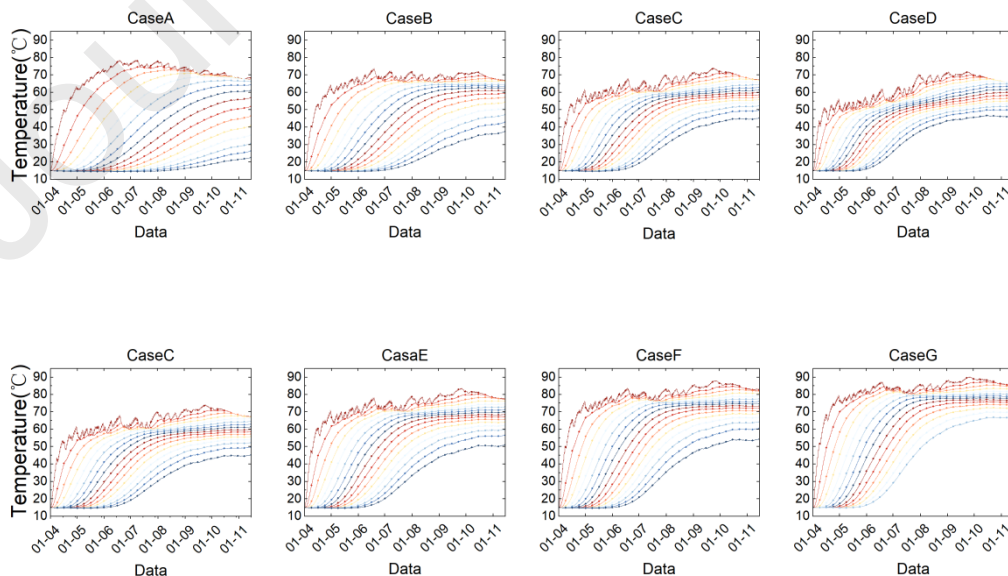
Table 6

583

System operating parameters under different energy charge modes

	Study on the effect of the flowrate			Study on the effect of collector area			
	CaseA	CaseB	CaseD	CaseC	CaseE	CaseF	CaseG
Flowrate (kg/s)	0.82*0.5	0.82*0.75	0.82*1.25	0.82	0.82	0.82	0.82
Collector Area (m ²)	2000	2000	2000	2000	3000	4000	5000
θ	60	60	60	60	60	60	60

584



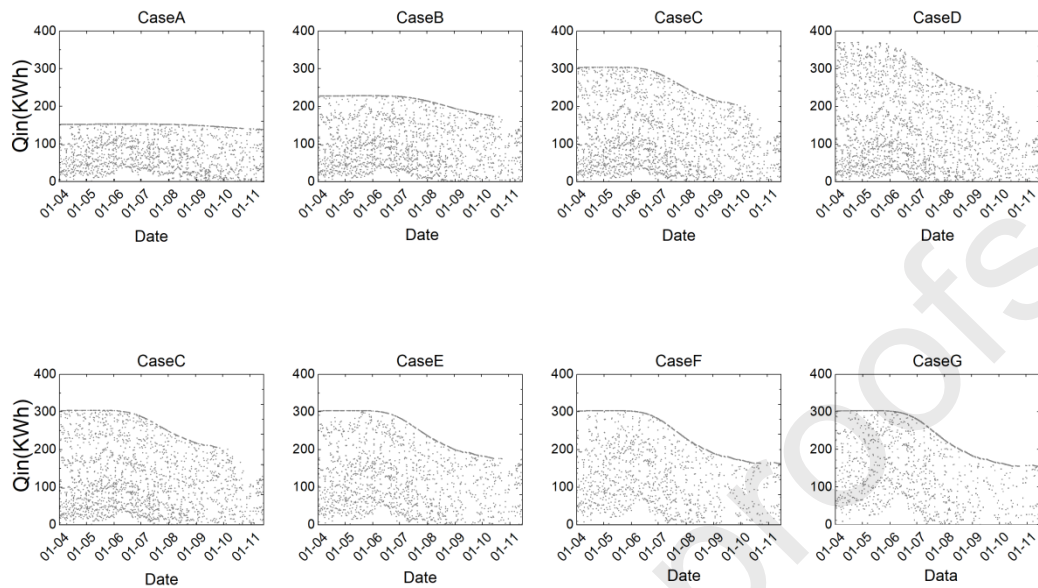
585

586

Fig 23 Changes in the temperature of the water in the pit under different energy charge cases

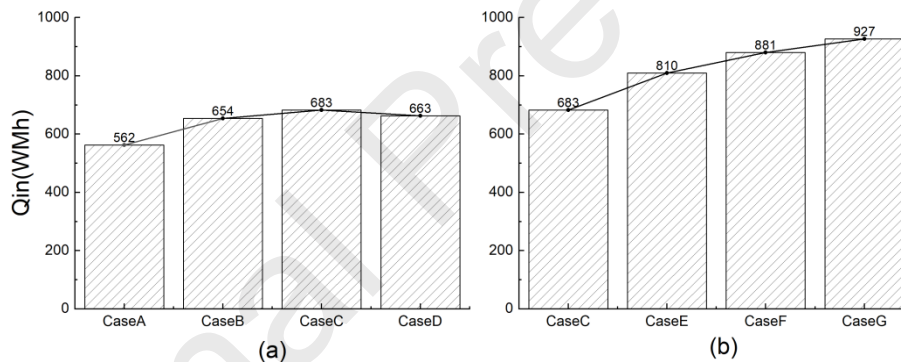
587

588



589

590

Fig 24 Changes in the energy charged into the pit in the first year under different energy charge cases

591

592

Fig 25-21 The total energy charged into STES under different cases

593

Fig. 23-A-3 shows the water temperature changes over time in each Case, it can be seen that, under the condition that other conditions do not change, if the flowrate of the water at the time of charging is increased, the temperature response time of the bottom water is also shorter. As a result, **Fig. 24-A-4** shows that the rapid response of the bottom layer temperature will also cause a corresponding drop in the efficiency of the solar collector. In **Case D** of **Fig. 24A-4**, The water flow into the solar collector is too large, which makes the solar collector unable to operate at full load. On the contrary, the total charged energy will be reduced, as can be seen in **CaseD** of **Fig. 2521**.

599

With the increase of the solar collector area, the increment is the largest when the collector area is 3000m², and then the total charge energy increment decreases with the increase of the collector area. Enlarging the collector area can certainly increase the total energy in the charging stage of the entire system, but under the condition of a certain flowrate, there is a limit to the temperature of the water, so the expansion of the collector area should not be blindly pursued, as shown in figure (b) of **Fig. 2521**. The collector-storage ratio is obtained by dividing the volume of the pit by the area of the solar collector. When the solar collector area is 3000 m²³, this model can achieve a relatively economical and efficient state and the corresponding collector-storage ratio is around 3768L/m².

606

607 **5. Conclusions**

608 In order to study the thermal efficiency of STES, a simplified numerical model of a cylindrical underground pit
609 was developed. The one-dimensional model is used to calculate the pit water region, the two-dimensional model is
610 used to calculate the soil region, and the model is verified by the typical daily charging and discharging experimental
611 data of the Huangdicheng Project. The temperature difference between the numerical model results and the
612 experimental results is acceptable. The model was subsequently implemented as a STES simulation model to further
613 study the depth-to-diameter ratio, the effect of the residual water temperature after one operation cycle on the heat
614 collection efficiency in the next year, and the effect of the initial charging mode and the collector-storage ratio on
615 the water temperature rise. The main results include:

- 616 1. In the first year of operation, the total heat collection energy of the 11304m³ pit is about 683MWh, of
617 which the energy discharged is 145MWh, the total heat loss is 180 MWh, the internal energy increase is
618 358 MWh, thus, the system storage efficiency is about 73.65%.
- 619 2. In the one-year operation, in the entire STES system, the thermal impact radius of the external
620 environment on the soil is about 8m, while the thermal impact radius of the water on the surrounding soil
621 is about 12m.
- 622 3. For the cylinder model of the 11304m³ pit, In order to obtain a relatively good system efficiency, it is
623 recommended that the depth-diameter ratio be about 0.343, and the system efficiency is up to 74% at this
624 depth-diameter ratio. When the depth-diameter ratio deviates from this value, as the deviation increases,
625 the system efficiency will also decrease rapidly.
- 626 4. At the end of the discharge phase of the STES system, the higher the residual water temperature of the
627 system, the lower the efficiency of the system collector in the following year, and the energy charged will
628 also decrease. During operation, try to release enough heat in the energy discharging stage. which is of
629 great significance for improving the system efficiency in the following year and reducing the total heat
630 loss.
- 631 5. In the case of setting the inclination angle of the solar collector at 60 degrees, for the cylinder model of
632 the 11304m³ pit, the relatively economical collector-storage ratio is 3768L/m². In addition, the inflow rate
633 of water has a significant influence on the solar collector and the change of the water temperature of
634 STES. in this model, the relatively optimal charging flow rate should be set at around 1.64kg/s.

635 **Author statement**

636 Guozhi Xu: Conceptualization, Formal analysis, Methodology, Software, Visualization, Writing - original draft

637 Lei Hu: Methodology, Formal analysis, Writing - review & editing

638 Yongqiang Luo: Conceptualization, Formal analysis, Methodology, Software, Visualization, Writing - original
639 draft

640 Zhiyong Tian: Methodology, Funding acquisition, Formal analysis, Writing - review & editing

641 Jie Deng: Methodology, Formal analysis, Writing - review & editing

642 Guofeng Yuan: Methodology, Formal analysis, Writing - review & editing

643 Jianhua Fan: Methodology, Formal analysis, Writing - review & editing

644

645 **Acknowledgments**

646 This study is supported by National Key R&D Program of China (No. 2021YFE0113500); the National Natural
 647 Science Foundation of China (No. 52008182).
 648

649 **Nomenclature**650 **Latin Symbols**

651	A	Cross-section area, [m ²]
652	C _p	Specific heat capacity, [J/(kg·K)]
653	Dep, d	calculation depth, [m]
654	D	Diameter, [m]
655	E	Energy content, [J]
656	h	heat transfer coefficient, [W/m ² °C]
657	H	height, m
658	I _g	Global Irradiance, [W/m ²]
659	m	flow rate, [kg/s]
660	M _p	energy-momentum, [J·m]
661	Q	heat flow, [W]
662	r	radial direction, [m]
663	R	Thermal resistance, [°C/ W]
664	Str	Stratification number, [-]
665	T	temperature, [°C]
666	u	wind velocity, [m/s]
667	V	volume, [m ³]
668	Z	vertical direction, [m]

669 **Greek Symbols**

670	δ	thickness, [m]
671	Δ	difference, [-]
672	φ	absorption factor of ground surface, [-]
673	η	energy efficiency, [-]
674	θ	Slope, [°]
675	λ	thermal conductivity, [W/m°C]
676	ρ	density, kg/m ³
677	τ	time, [s]

678 **Subscripts**

679	1	The first unit to be calculated
680	2	The second unit to be calculated

681	3	The third unit to be calculated
682	ave	average
683	a	air
684	bot	bottom
685	c	solar collector
686	ci	water flowing into the solar collector
687	co	water flowing out the solar collector
688	ch	charging
689	con	concrete
690	disc	discharging
691	ev	environment
692	exp	experiment
693	G	ground
694	i, j, k	number of elements
695	in	water flowing into the pit
696	ins	insulation
697	L	light
698	loss	heat loss
699	num	numeric
700	OB	Obliquely
701	p	pit
702	R	right
703	s	soil
704	t	time
705	U	up
706	w	water

707 **Appendix A.- Supplementary material**

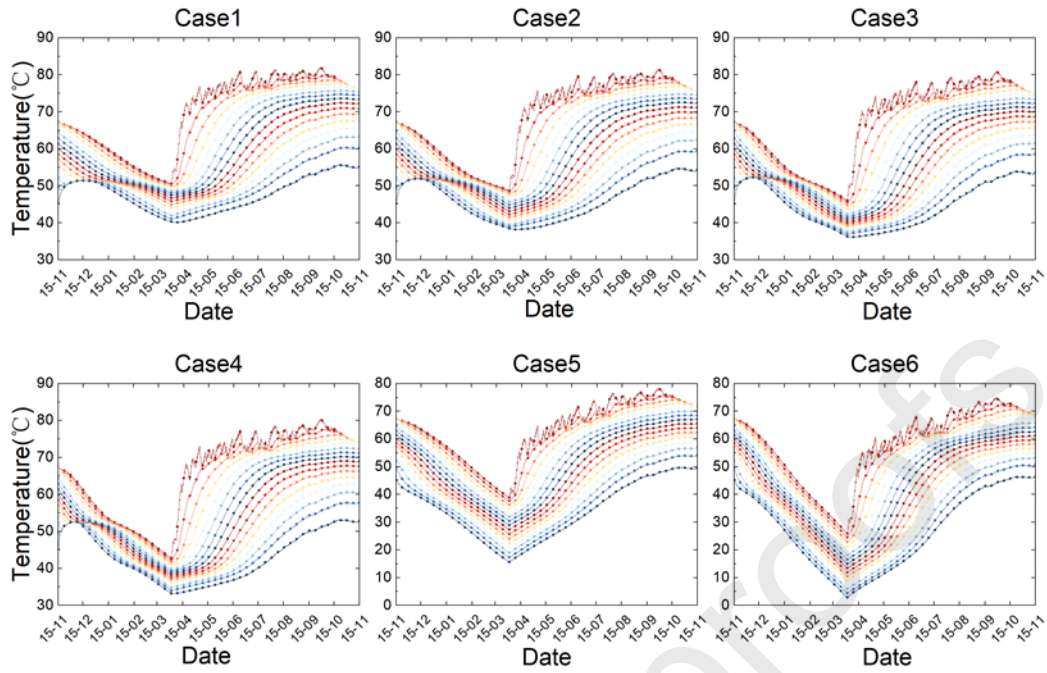
708 **Fig. A-1 and Fig. A-2 are the temperature change curve of water in different modes and the hourly charging**
709 **scatter diagram of the collector in the discharging stage.**

710 **Fig. A-3 and Fig. A-4 are the temperature change curve of water in different modes and the hourly charging**
711 **scatter diagram of the collector in the charging stage.**

712

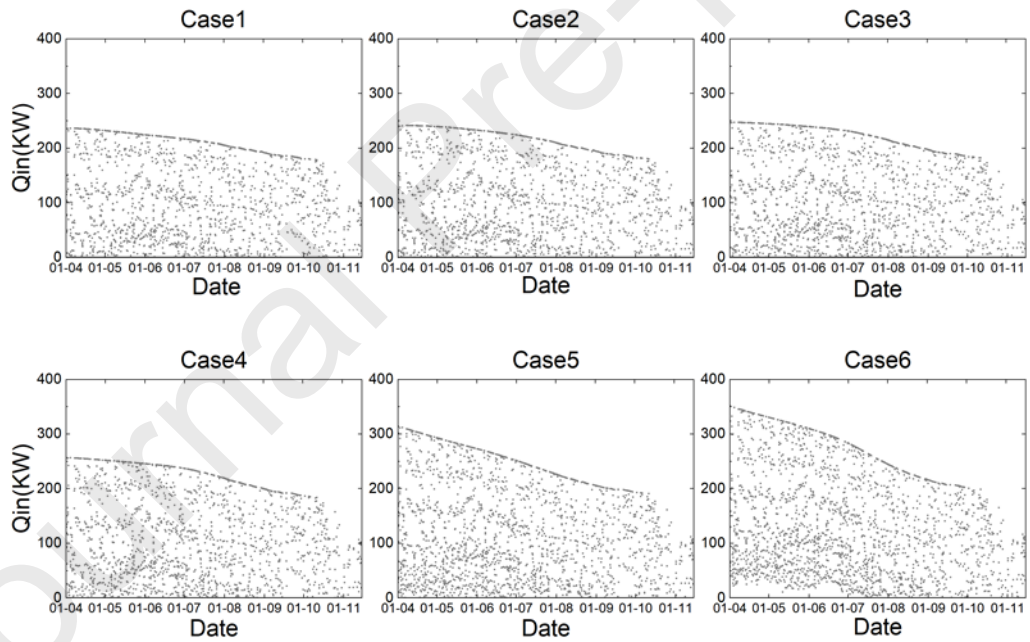
713

714



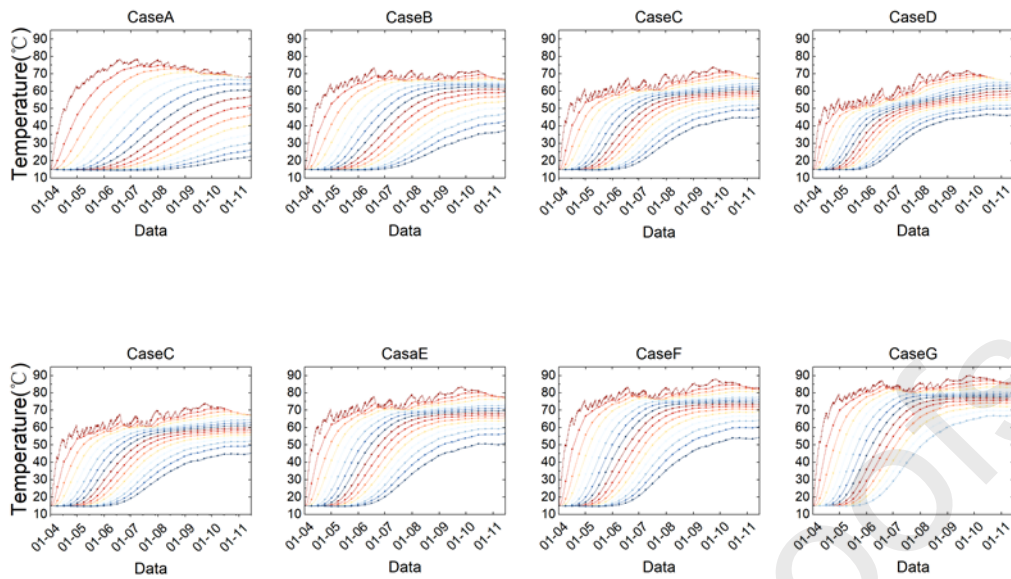
715
716

Fig A-1 Changes in the temperature of the water in the pit under different energy discharge cases



717
718

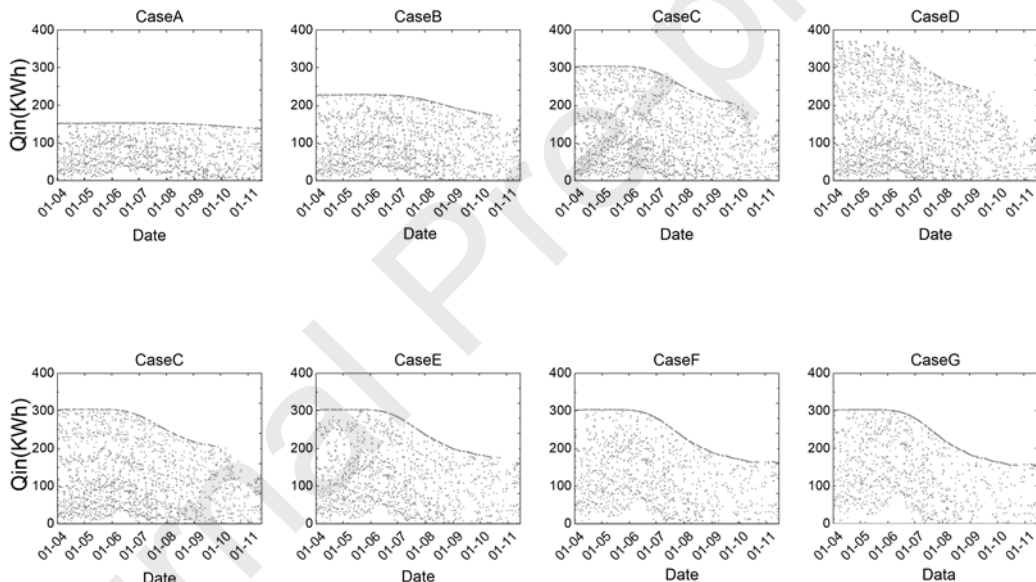
Fig A-2 Changes in the energy charged into the pit in the second year under different energy discharge cases



719

720

Fig A-3 Changes in the temperature of the water in the pit under different energy charge cases



721

722

723

Fig A-4 Changes in the energy charged into the pit in the first year under different energy charge cases

724

References

725 [1]J. Wang, Z. Zhou, J. Zhao, J. Zheng, Z. Guan, Towards a cleaner domestic heating sector in China: Current

726 situations, implementation strategies, and supporting measures, Applied Thermal Engineering 152 (2019) 515-531.

727 <https://doi.org/10.1016/j.applthermaleng.2019.02.117>

728 [2]J. Fan, J. Huang, A. Chatzidiakos, S. Furbo, Experimental and theoretic investigations of thermal behavior

729 of a seasonal water pit heat storage, ISES Solar World Conference 2017 and the IEA SHC Solar Heating and

730 Cooling Conference for Buildings and Industry 2017 (2017). <http://dx.doi.org/10.18086/swc.2017.13.03>

- 731 [3]B. Stutz, N. Le Pierres, F. Kuznik, K. Johannes, E. Palomo Del Barrio, J.-P. Bédécarrats, S. Gibout, P.
732 Marty, L. Zalewski, J. Soto, N. Mazet, R. Olives, J.-J. Bezian, D.P. Minh, Storage of thermal solar energy,
733 Comptes Rendus Physique 18 (2017) 401-414. <https://doi.org/10.1016/j.crhy.2017.09.008>
- 734 [4]M. Guadalfajara, M.A. Lozano, L.M. Serra, Simple calculation tool for central solar heating plants with
735 seasonal storage, Solar Energy 120 (2015) 72-86. <https://doi.org/10.1016/j.solener.2015.06.011>
- 736 [5]W. Zheng, Y. Zhang, J. Xia, Y. Jiang, Cleaner heating in Northern China: potentials and regional balances,
737 Resources, Conservation and Recycling 160 (2020) 104897. <https://doi.org/10.1016/j.resconrec.2020.104897>
- 738 [6]Y. Luo, N. Cheng, S. Zhang, Z. Tian, G. Xu, X. Yang, J. Fan, Comprehensive energy, economic,
739 environmental assessment of a building integrated photovoltaic-thermoelectric system with battery storage for net
740 zero energy building, Building Simulation 15 (2022) 1923-1941. <https://doi.org/10.1007/s12273-022-0904-1>.
- 741 [7]J. Xu, R.Z. Wang, Y. Li, A review of available technologies for seasonal thermal energy storage, Solar
742 Energy 103 (2014) 610-638. <https://doi.org/10.1016/j.solener.2013.06.006>
- 743 [8]P. Pinel, C.A. Cruickshank, I. Beausoleil-Morrison, A. Wills, A review of available methods for seasonal
744 storage of solar thermal energy in residential applications, Renewable and Sustainable Energy Reviews 15 (2011)
745 3341-3359. <https://doi.org/10.1016/j.rser.2011.04.013>
- 746 [9]A. Hesarakı, S. Holmberg, F. Haghghat, Seasonal thermal energy storage with heat pumps and low
747 temperatures in building projects—A comparative review, Renewable and Sustainable Energy Reviews 43 (2015)
748 1199-1213. <https://doi.org/10.1016/j.rser.2014.12.002>
- 749 [10]K.S. Lee, A Review on Concepts, Applications, and Models of Aquifer Thermal Energy Storage Systems,
750 Energies 3 (2010). <http://dx.doi.org/10.3390/en3061320>
- 751 [11]A.V. Novo, J.R. Bayon, D. Castro-Fresno, J. Rodriguez-Hernandez, Review of seasonal heat storage in
752 large basins: Water tanks and gravel–water pits, Applied Energy 87 (2010) 390-397.
753 <https://doi.org/10.1016/j.apenergy.2009.06.033>
- 754 [12]N. Catolico, S. Ge, J.S. McCartney, Numerical Modeling of a Soil-Borehole Thermal Energy Storage
755 System, Vadose Zone Journal 15 (2016). <https://doi.org/10.2136/vzj2015.05.0078>
- 756 [13]Y. Bai, Z. Wang, J. Fan, M. Yang, X. Li, L. Chen, G. Yuan, J. Yang, Numerical and experimental study
757 of an underground water pit for seasonal heat storage, Renewable Energy 150 (2020) 487-508.
758 <https://doi.org/10.1016/j.renene.2019.12.080>
- 759 [14]I. Sarbu, C. Sebarchievici, Solar Heating and Cooling Systems: Fundamentals, experiments and
760 applications, 2016.
- 761 [15]X. Pan, Y. Xiang, M. Gao, J. Fan, S. Furbo, D. Wang, C. Xu, Long-term thermal performance analysis of
762 a large-scale water pit thermal energy storage, Journal of Energy Storage 52 (2022) 105001.
763 <https://doi.org/10.1016/j.est.2022.105001>
- 764 [16]C. Chang, Z. Wu, H. Navarro, C. Li, G. Leng, X. Li, M. Yang, Z. Wang, Y. Ding, Comparative study of
765 the transient natural convection in an underground water pit thermal storage, Applied Energy 208 (2017) 1162-
766 1173. <https://doi.org/10.1016/j.apenergy.2017.09.036>
- 767 [17]C. Chang, B. Nie, G. Leng, C. Li, X. She, X. Peng, J. Deng, Influences of the key characteristic
768 parameters on the thermal performance of a water pit seasonal thermal storage, Energy Procedia 142 (2017) 495-
769 500. <https://doi.org/10.1016/j.egypro.2017.12.077>
- 770 [18]J. Fan, J. Huang, A. Chatzidiakos, S. Furbo, Experimental and theoretic investigations of thermal
771 behavior of a seasonal water pit heat storage, (2017). <http://dx.doi.org/10.18086/swc.2017.13.03>
- 772 [19]K. Narula, F.D.O. Filho, J. Chambers, M.K. Patel, Simulation and comparative assessment of heating
773 systems with tank thermal energy storage – A Swiss case study, Journal of Energy Storage 32 (2020) 101810.
774 <https://doi.org/10.1016/j.est.2020.101810>

- 775 [20]M. Jradi, C. Veje, B.N. Jørgensen, Performance analysis of a soil-based thermal energy storage system
776 using solar-driven air-source heat pump for Danish buildings sector, Applied Thermal Engineering 114 (2017)
777 360-373. <https://doi.org/10.1016/j.applthermaleng.2016.12.005>
- 778 [21]K. Kubiński, Ł. Szablowski, Dynamic model of solar heating plant with seasonal thermal energy storage,
779 Renewable Energy 145 (2020) 2025-2033. <https://doi.org/10.1016/j.renene.2019.07.120>
- 780 [22]S. Raab, D. Mangold, H. Müller-Steinhagen, Validation of a computer model for solar assisted district
781 heating systems with seasonal hot water heat store, Solar Energy 79 (2005) 531-543.
782 <https://doi.org/10.1016/j.solener.2004.10.014>
- 783 [23]A. Dahash, M.B. Janetti, F. Ochs, Detailed Axial Symmetrical Model of Large-Scale Underground
784 Thermal Energy Storage, COMSOL 2018 Conference Lausanne (2018).
- 785 [24]F. Ochs, A. Dahash, A. Tosatto, M. Bianchi Janetti, Techno-economic planning and construction of cost-
786 effective large-scale hot water thermal energy storage for Renewable District heating systems, Renewable Energy
787 150 (2020) 1165-1177. <https://doi.org/10.1016/j.renene.2019.11.017>
- 788 [25]A. Dahash, F. Ochs, A. Tosatto, W. Streicher, Toward efficient numerical modeling and analysis of large-
789 scale thermal energy storage for renewable district heating, Applied Energy 279 (2020) 115840.
790 <https://doi.org/10.1016/j.apenergy.2020.115840>
- 791 [26]P.J. Ryan, D.R.F. Harleman, K.D. Stolzenbach, Surface heat loss from cooling ponds, Water Resources
792 Research 10 (1974) 930-938. <https://doi.org/10.1029/WR010i005p00930>
- 793 [27]B. Larwa, Heat Transfer Model to Predict Temperature Distribution in the Ground, Energies 12 (2019).
794 10.3390/en12010025
- 795 [28]Q. Qi, S. Deng, Y. Jiang, A simulation study on a solar heat pump heating system with seasonal latent
796 heat storage, Solar Energy 82 (2008) 669-675. <https://doi.org/10.1016/j.solener.2008.02.017>
- 797 [29]J. Fernández-Seara, F.J. Uhl' a, J. Sieres, Experimental analysis of a domestic electric hot water storage
798 tank. Part II: dynamic mode of operation, Applied Thermal Engineering 27 (2007) 137-144.
799 <https://doi.org/10.1016/j.applthermaleng.2006.05.004>
- 800 [30]A. Castell, M. Medrano, C. Solé, L.F. Cabeza, Dimensionless numbers used to characterize stratification
801 in water tanks for discharging at low flow rates, Renewable Energy 35 (2010) 2192-2199.
802 <https://doi.org/10.1016/j.renene.2010.03.020>

803

804 **Declaration of interests**

805

806 The authors declare that they have no known competing financial interests or personal relationships that
807 could have appeared to influence the work reported in this paper.

808

809 The authors declare the following financial interests/personal relationships which may be
810 considered as potential competing interests:

811

812

813

814

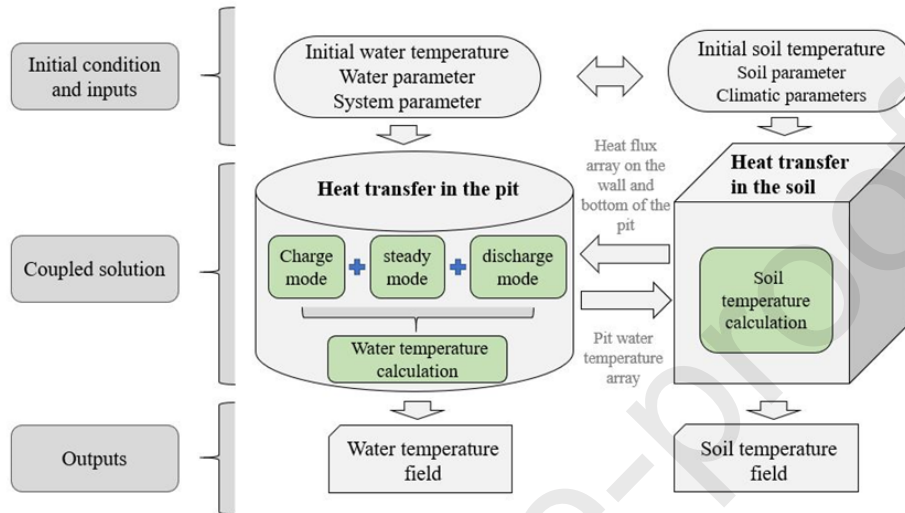
815

816

817

818

Graphical Abstract



819

820

821